ACS NANO

www.acsnano.org

ARTICLE

Rational Construction of a Ni/$CoMoO_4$ Heterostructure with Strong Ni−O−Co Bonds for Improving Multifunctional Nanozyme Activity

Yang Dang, Guangtu Wang, Gehong Su, Zhiwei Lu, Yanying Wang, Tao Liu, Xiang Pu, Xianxiang Wang, Chun Wu, Chang Song, Qingbiao Zhao,* Hanbing Rao,* and Mengmeng Sun*

Cite This: *ACS Nano* 2022, 16, 4536−4550

Read Online

ACCESS | Metrics & More | Article Recommendations | Supporting Information

ABSTRACT: Due to the lack of a general descriptor to predict the activity of nanomaterials, the current exploration of nanozymes mainly depended on trial-and-error strategies, which hindered the effective design of nanozymes. Here, with the help of a large number of Ni−O−Co bonds at the interface of heterostructures, a prediction descriptor was successfully determined to reveal the double enzyme-like activity mechanisms for Ni/$CoMoO_4$. Additionally, DFT calculations revealed that interface engineering could accelerate the catalytic kinetics of the enzyme-like activity. Ni−O−Co bonds were the main active sites for enzyme-like activity. Finally, the colorimetric signal and intelligent biosensor of Ni/$CoMoO_4$ based on deep learning were used to detect organophosphorus and ziram sensitively. Meanwhile, the *in situ* FTIR results uncovered the detection mechanism: the target molecules could block Ni−O−Co active sites at the heterostructure interface leading to the signal peak decreasing. This study not only provided a well design strategy for the further development of nanozymes or other advanced catalysts, but it also designed a multifunctional intelligent biosensor platform. Furthermore, it also provided preferable ideas regarding the catalytic mechanism and detection mechanism of heterostructure nanozymes.

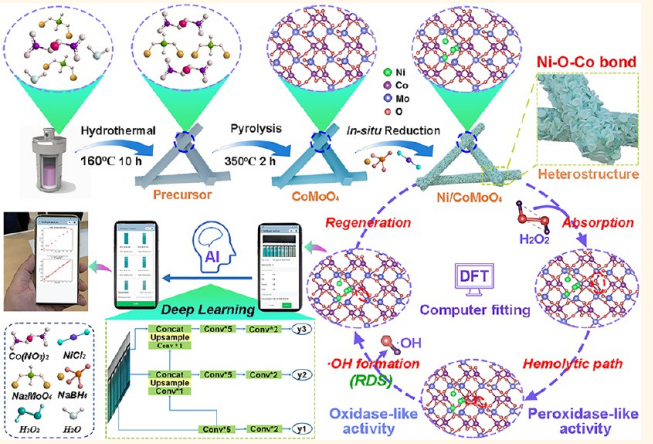

KEYWORDS: *interface engineering, heterostructure nanozymes, catalytic mechanism, intelligent biosensor, multifunctional application*

INTRODUCTION

In recent years, due to the shortcomings of natural enzymes, for instance their ease of inactivation and high storage cost, the development of nanozymes has been promoted. Nanozymes are a kind of nanomaterials with enzyme-like activity[1−3] which have attracted increasing interest and been widely used in analytical detection, medical diagnosis, and biosensing.[3−6] Inspired by natural enzymes, many nanomaterials have been proven to have the activities of oxidase,[4] peroxidase,[7] laccase,[8,9] and dehydrogenases,[10] for example, metal organic frameworks (MOFs),[11] metallic oxide,[12] and metal molybdate compounds and their corresponding complexes.[13] Unfortunately, due to the lack of predictable descriptors, the current exploration of nanozyme activity is mainly through trial-and-error strategies.[14] The relationship between the structure and enzyme-like activity is poorly understood, which greatly hinders the design of nanozymes. Thus, it is crucial to investigate the structure−activity relationships in-depth and clarify the key factors of nanozyme catalytic activity.[15−19] This is of great guiding significance for the rational design of efficient nanozymes, revealing the mechanisms and broadening the application scope of nanozymes.

Metal molybdate compounds $MMoO_4$ (M = Co and Ni) have attracted great interest due to their merits of nontoxicity, low cost, and better redox activity.[20,21] However, compared

Received: December 11, 2021
Accepted: February 28, 2022
Published: March 3, 2022

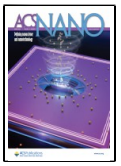

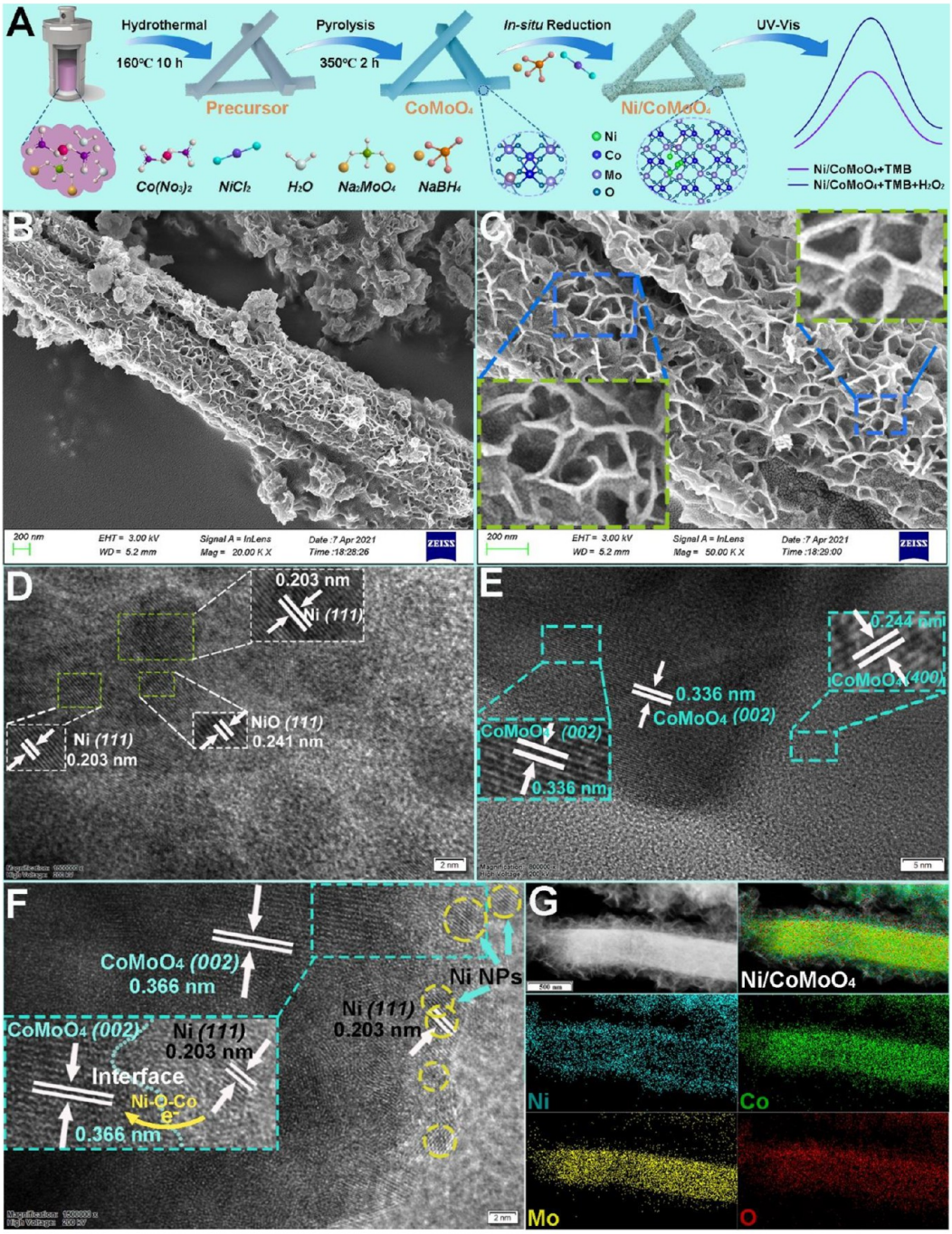

Figure 1. (A) Schematic diagram of Ni/$CoMoO_4$ synthesis. (B and C) SEM images of Ni/$CoMoO_4$. HRTEM images of (D) Ni NPs, (E) $CoMoO_4$, and (F) Ni/$CoMoO_4$. (G) TEM mapping images of Ni/$CoMoO_4$.

with other $MMoO_4$ compounds, numerous studies of $CoMoO_4$ are mainly focused on its use as a supercapacitor,[21] while there are few reports on enzyme-like catalysis because of its poor catalytic performance. In particular, interface engineering is considered to be one of the most potential methods to accelerate catalytic kinetics.[22] Thus, the introduction of appropriate metals into $CoMoO_4$ can improve the intrinsic catalytic activity by heterostructure engineering.[23,24] For one thing, an appropriate interface engineering can promote the electron transfer and redistribution.[23,25] For another, the distinctive atomic coordination at the interface will greatly modify the catalytic activity.[26] In addition, the partial delocalization of spin status at the interface through the bridging O^{2-} results in a synergistic effect of the heterogeneous interface.[27,28] This provides the possibility to break the scaling relationship, which is a key factor for promoting the catalytic performance.[19,23,24]

It is well-known that the splitting of 3d orbitals and the corresponding electronic coupling will lead to electron imbalance and consequently partial electron transfer.[29] According to refs 28−31, Ni with the similar electron arrangement state to and higher electronegativity (1.91) than Co (1.88) has an ability to transfer electrons to Co, which will stimulate the redox ability of Co elements to enhance the

https://doi.org/10.1021/acsnano.1c11012
ACS Nano 2022, 16, 4536−4550

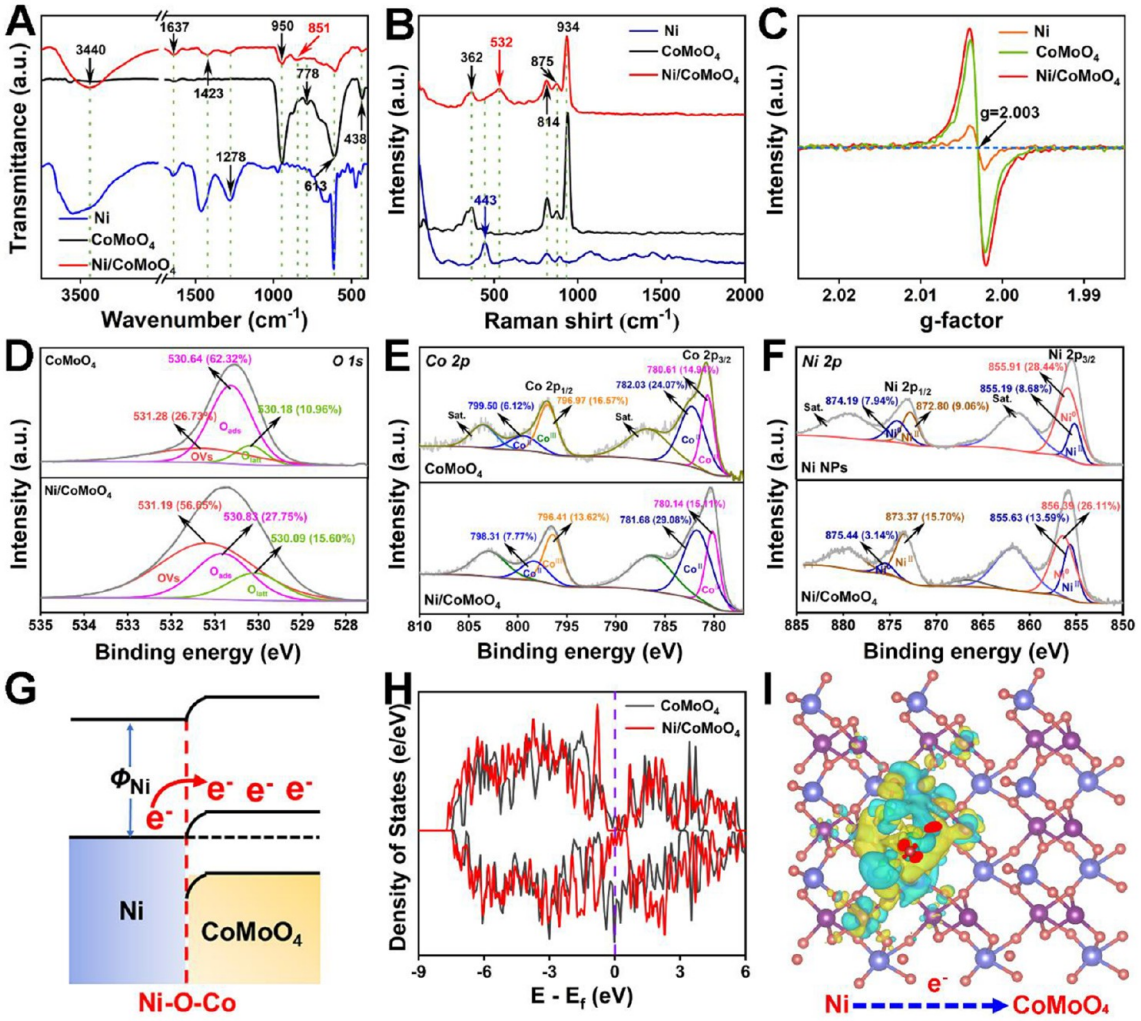

Figure 2. (A) FTIR spectra, (B) Raman spectra, and (C) ESR spectra of Ni, $CoMoO_4$, and Ni/$CoMoO_4$. (D–F) XPS spectra of (D) O 1s and (E) Co 2p of $CoMoO_4$ and Ni/$CoMoO_4$ and (F) Ni 2p of Ni and Ni/$CoMoO_4$. (G) Energy band structure diagram of Ni/$CoMoO_4$. (H) Density of states on the $CoMoO_4$ and Ni/$CoMoO_4$ systems. (I) Differential charge density in the Ni–O–Co bonds at the Ni/$CoMoO_4$ heterostructure interface.

catalytic activity. Moreover, Ni doping significantly enhances the intrinsic activity of the active site by redistribution of charge density and interaction of Co metal elements.[32−34] Most importantly, local electron distribution may occur by bridging O^{2-} (π-donation) owing to the different t_{2g} d-orbitals of Ni and Co species at the interface.[28] In the interface of nanocomposites with aggregation of Ni and Co, after acceptance of the partial electrons from Ni^0 *via* the bridging O^{2-}, the t_{2g} d-orbitals of Co^{3+} will be in the electron-rich status, which will accelerate the charge transfer.[35] Meanwhile, the obtained e^- tends to transfer from Ni^0 to Co^{3+}.[36] Therefore, the π-symmetric electrons between Ni and Co will be optimally redistributed in the favorable direction due to the spontaneous electron transfer, which will be the key factor to accelerate the kinetics of the catalytic reaction.[28,35,37] Besides, the rapid electron transfer of Ni, Co-based nanocomposites existed because of their metal properties and well adjustable microstructure.[29]

Therefore, Ni as the most suitable element was introduced on the surface of $CoMoO_4$ to construct a heterostructure interface with a large number of Ni–O–Co bonds to promote electron transfer by the interface engineering strategy. It broke the scaling relationship with the help of a large number of Ni–O–Co bonds at the interface and presented the efficient double enzyme-like activity and multifunctional application. Besides, benefiting from the interfacial engineering strategy, Ni/$CoMoO_4$ also exhibited excellent intelligent biosensor stability based on deep learning. Meanwhile, theoretical calculations and *in situ* FTIR were implemented to systematically explore the catalytic mechanism and the structure–activity relationship. Most importantly, this was an excellent strategy to enhance the catalytic activity of nanozymes by regulating the formation of chemical bonds. This might be one of the important explorations of metal molybdate complexes in the field of enzyme-mimicking catalysis in the near future, and it would also provide a promising ideal for the efficient design of nanozymes.

RESULTS AND DISCUSSION

Characterization. The specific surface area and pore size distribution of $CoMoO_4$ and Ni/$CoMoO_4$ were measured through BET. Compared to $CoMoO_4$ (20.53 $m^2\ g^{-1}$), Ni/$CoMoO_4$ exhibited a larger surface area of about 117.9 $m^2\ g^{-1}$ (Figure S1A). This was due to *in situ* growth of Ni

https://doi.org/10.1021/acsnano.1c11012
ACS Nano 2022, 16, 4536−4550

nanoparticles (Ni NPs) on $CoMoO_4$, and more honeycomb-like voids were formed on the Ni/$CoMoO_4$ surface. The pore size distribution of Ni/$CoMoO_4$ from 3 to 40 nm increased obviously than that of $CoMoO_4$ (Figure S1B). Meanwhile, the synthesis process of Ni/$CoMoO_4$ is fully described in Figure 1A. Significantly, the large surface area and rich pores would offer sufficient active sites and promote the adsorption of more substrates.

The morphology and structure of Ni NPs, $CoMoO_4$, and Ni/$CoMoO_4$ were confirmed by scanning electron microscope (SEM) and transmission electron microscopy (TEM). The Ni catalysts with many voids were formed by small particle size Ni NPs (Figure S2A), while $CoMoO_4$ exhibited a smooth surface and regular layered cubic structure (Figure S2B and C). After Ni NPs were *in situ* grown on $CoMoO_4$, the layered cubic structure of $CoMoO_4$ could still be kept, and many empty cavities like a honeycomb were found on the surface of Ni/$CoMoO_4$ (Figure 1B and C). Compared with Ni NPs (Figure S2D) and $CoMoO_4$ (Figure S2E), it could be seen clearly in TEM images of Ni/$CoMoO_4$ that there were a lot of uniform nanoparticles (yellow circles) growing on $CoMoO_4$ (Figure S2F). Moreover, to further analyze the lattice states of Ni NPs, $CoMoO_4$, and Ni/$CoMoO_4$, high-resolution transmission electron microscopy (HRTEM) was investigated. For Ni NPs, the lattice spacing of 0.203 nm was attributed to the Ni(111) plane (Figure 1D), and for $CoMoO_4$, the interplanar spacings of 0.336 and 0.244 nm were consistent with the $CoMoO_4$(002) and $CoMoO_4$(200) planes, respectively (Figure 1E). Notably, the Ni(111) and $CoMoO_4$(002) planes could be observed in two adjacent particles. Besides, it is worth noting that there was a tight interface between Ni NPs and $CoMoO_4$ (Figure 1F, blue line), which ensured the formation of intimate contact between Ni NPs and $CoMoO_4$ to facilitate charge transfer. It might play an important role as an active site in improving catalytic performance. Meanwhile, the corresponding element mapping disclosed that Ni, Co, Mo, and O were uniformly dispersed over the whole Ni/$CoMoO_4$ (Figure 1G).

The crystal phase of Ni/$CoMoO_4$ was characterized by X-ray diffraction (XRD) to further prove the successful synthesis of Ni/$CoMoO_4$. As depicted in Figure S3A, according to PDF#04-0850, the diffraction peaks of Ni at 44.51°, 51.85°, and 76.37° could be indexed to (111), (200), and (220), respectively. In addition, the peaks at 37.25°, 43.28°, and 62.88° were attributed to NiO (PDF#47-1049), indicating Ni and Ni oxides coexisted in single Ni NPs. For $CoMoO_4$, some main peaks located at 23.33° and 26.51° corresponded to the (021) and (002) crystal planes of $CoMoO_4$ (PDF#21-0868), respectively (Figure S3B). As for Ni/$CoMoO_4$, the diffraction peaks of $CoMoO_4$ are displayed in Figure S3C. However, the corresponding characteristic peaks of Ni NPs were not shown in the XRD spectra, which is attributed to two main reasons. One reason was that Ni was uniformly dispersed on the surface of $CoMoO_4$, as could see from the TEM results (Figure S2F). The other reason was the Ni could be etched in the Ni/$CoMoO_4$ synthetic process. As shown by the inductively coupled plasma (ICP) measurement, the content of Ni was only 5.58 wt %, much lower than the addition (Table S1).

Fourier transform infrared spectroscopy (FTIR) further confirmed the hybridization characteristics of Ni/$CoMoO_4$. In Figure 2A, for Ni NPs, the peak at 500−636 cm^{-1} belonged to the bending vibration of Ni-OH, indicating the existence of oxidation states in Ni NPs, and two main bands were observed in the $CoMoO_4$ spectra at 613 and 950 cm^{-1}, corresponding to the Co−O and Mo−O−Mo vibration modes. The peak at 438 cm^{-1} belonged to the vibration of the CoO_6 and MoO building groups.[38] For Ni/$CoMoO_4$, the peaks near 1423 and 3440 cm^{-1} originated from the bending and stretching vibrations of OH, respectively. Significantly, the new peak appeared at 851 cm^{-1}, which was consistent with the Ni−O−Co vibration in Ni/$CoMoO_4$.[38,39] The results indicated that the interaction between Ni and $CoMoO_4$ at the heterostructure interface was conducive to the formation of Ni−O−Co bonds, which might be the active sites for nanozyme activity.

Raman spectroscopy was performed to further prove the Ni loading on $CoMoO_4$ and the interaction between Ni and Co. Figure 2B shows the Raman spectra of Ni NPs, $CoMoO_4$, and Ni/$CoMoO_4$; the diffraction peaks of Ni NPs at 443 cm^{-1} could be indexed to the Ni−O bond. The Raman spectra of pure $CoMoO_4$ had a strong characteristic peak at 934 cm^{-1}, and some peaks with medium intensity at 875, 814, and 362 cm^{-1} corresponded to the contraction vibration of Mo−O−Co.[40] For Ni/$CoMoO_4$, the change was observed near the band of 280−390 cm^{-1}, which was concerned with the asymmetric and symmetric bending model of O−Mo−O.[41] Most notably, a new characteristic peak could be observed at 532 cm^{-1}, which was assigned to the Ni−O−Co stretching/vibration in the spectrum of Ni/$CoMoO_4$.[42] It was further testified that there was an intense electronic interaction between Ni and $CoMoO_4$ at the interface, which was consistent with the FTIR. These results indicated that Ni/$CoMoO_4$ were successfully synthesized.

Furthermore, electron spin-resonance (ESR) spectroscopy provided convincing proof for revealing the change of oxygen vacancies (OVs). In Figure 2C, the ESR signals of samples could be observed at g = 2.002, which originated from the unpaired electrons of oxygen on the surface sample.[43,44] The ESR signal strength indicated that Ni/$CoMoO_4$ had more OVs than Ni and $CoMoO_4$. To quantitatively estimate the OV concentrations, the X-ray photoelectron spectroscopy (XPS) spectra were further adopted to fit the O 1s peaks of $CoMoO_4$ and Ni/$CoMoO_4$ (Figure 2D). For $CoMoO_4$, the peak at 530.18 eV was ascribed to the lattice oxygen (O_{latt}) bonds of metal oxides,[45] and that located at 530.64 eV was contacted to the hydroxyl oxygen adsorbed (O_{ads}) on the catalyst surface.[46,47] As could be further seen in Figure 2D, the peak at 531.28 eV might be owing to the defect site of low hypoxia coordination, indicating that OVs were created on the surface of $CoMoO_4$.[48,49] It is worth noting that the content of OVs for Ni/$CoMoO_4$ was calculated to be 56.65%, markedly higher than that for $CoMoO_4$ (26.73%). It is demonstrated that Ni incorporation could indeed produce more OVs, in line with the ESR result. Previous studies had shown that on the one hand, OVs could activate adsorbed oxygen and provide a lattice position for oxygen migration, resulting in the formation of electrophilic oxygen species with high catalytic activity. On the other hand, the defects also could be produced in the energy band gap of the Co-oxidation state, and the electrons in this defect state were easily activated, resulting in the catalytic activity being significantly improved.[50,51]

The XPS spectra of Ni, $CoMoO_4$, and Ni/$CoMoO_4$ were evaluated to reveal the mechanism of electron transfer (Figure S3D). As illustrated in Figure 2E, two signal peaks of $CoMoO_4$ at 796.97 and 780.61 eV were attributed to Co $2p_{1/2}$ and Co $2p_{3/2}$ of Co^{3+}. Besides, two characteristic peaks at 799.50 and 782.03 eV were assigned to Co^{2+} for Co $2p_{1/2}$ and Co $2p_{3/2}$.[52]

https://doi.org/10.1021/acsnano.1c11012
ACS Nano 2022, 16, 4536−4550

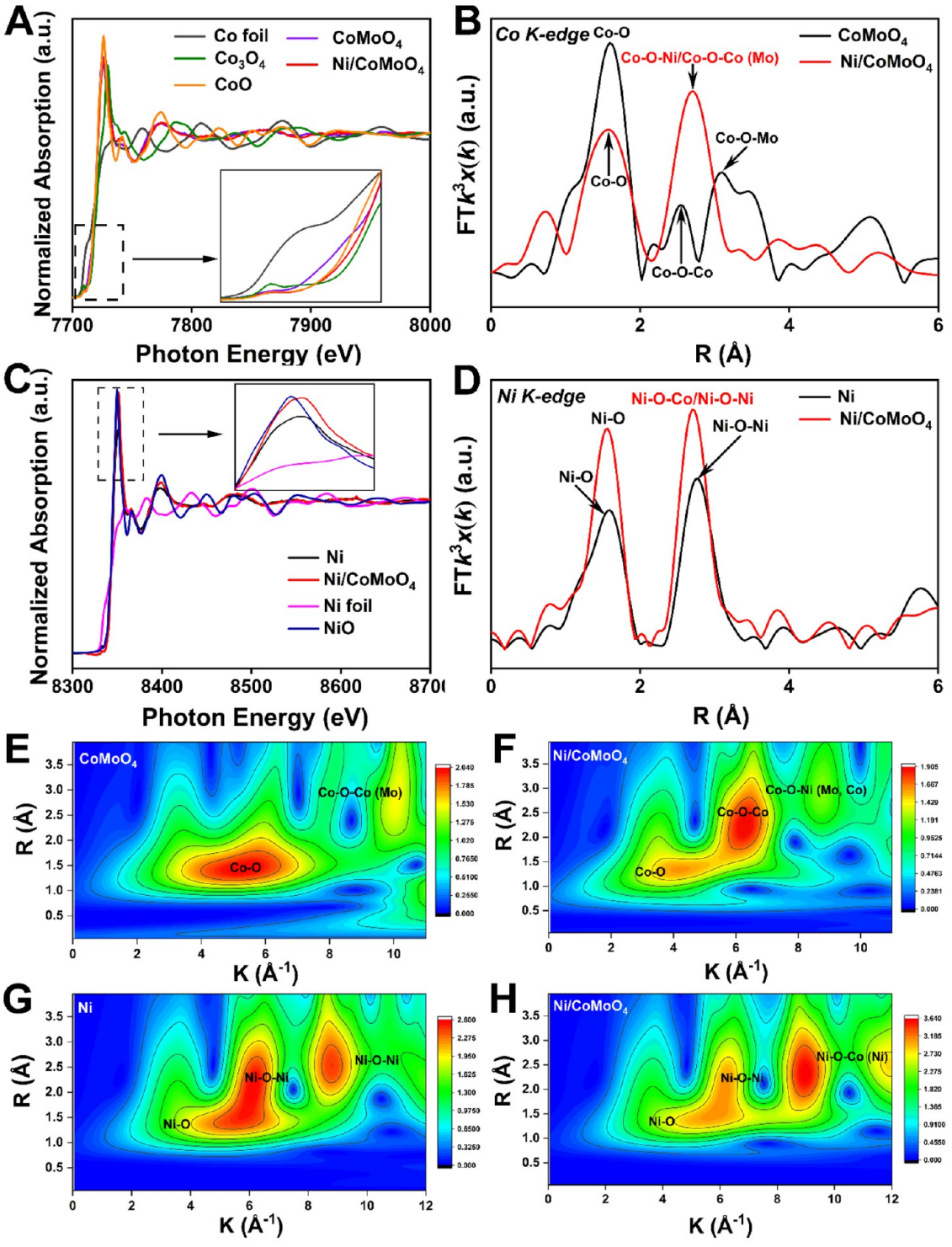

Figure 3. (A) Co K-edge XANES spectra of Co, CoO, Co_3O_4, $CoMoO_4$, and $Ni/CoMoO_4$. (B) Co K-edge EXAFS spectra of $CoMoO_4$ and $Ni/CoMoO_4$. (C) Ni K-edge XANES spectra of Ni foil, NiO, Ni, and $Ni/CoMoO_4$. (D) Ni K-edge EXAFS spectra of Ni and $Ni/CoMoO_4$. Co K-edge WT-EXAFS of (E) $CoMoO_4$ and (F) $Ni/CoMoO_4$. Ni K-edge WT-EXAFS of (G) Ni and (H) $Ni/CoMoO_4$.

Obviously, compared with $CoMoO_4$, $Ni/CoMoO_4$ (0.78) possessed decreased surface ratios of Co^{3+}/Co^{2+} than that of $CoMoO_4$ (1.04). This indicated that the electron density of $CoMoO_4$ was regulated with the addition of Ni elements. The XPS fitting peaks of Ni NPs (Figure 2F), the major Ni 2p peaks, were located at 874.19 and 855.91 eV, which was in accordance with the range for Ni 2p of metallic Ni. And the other two peaks were found at 872.80 and 855.19 eV, corresponding to the existence of Ni^{2+}.[53,54] Compared with the pure Ni NPs, the proportion of Ni^{2+} species increased significantly (8.87% → 14.65%) for $Ni/CoMoO_4$. These phenomena illustrated that there was a clear electron transfer from Ni^0 to Co^{3+} through the Ni−O−Co bridging oxygen bond, leading an enhanced ratio of Co^{2+}/Co^{3+}. The chemical shift was closely related to the Fermi energy, the work function, and the position of the energy band center.[55,56] It was

https://doi.org/10.1021/acsnano.1c11012
ACS Nano 2022, 16, 4536−4550

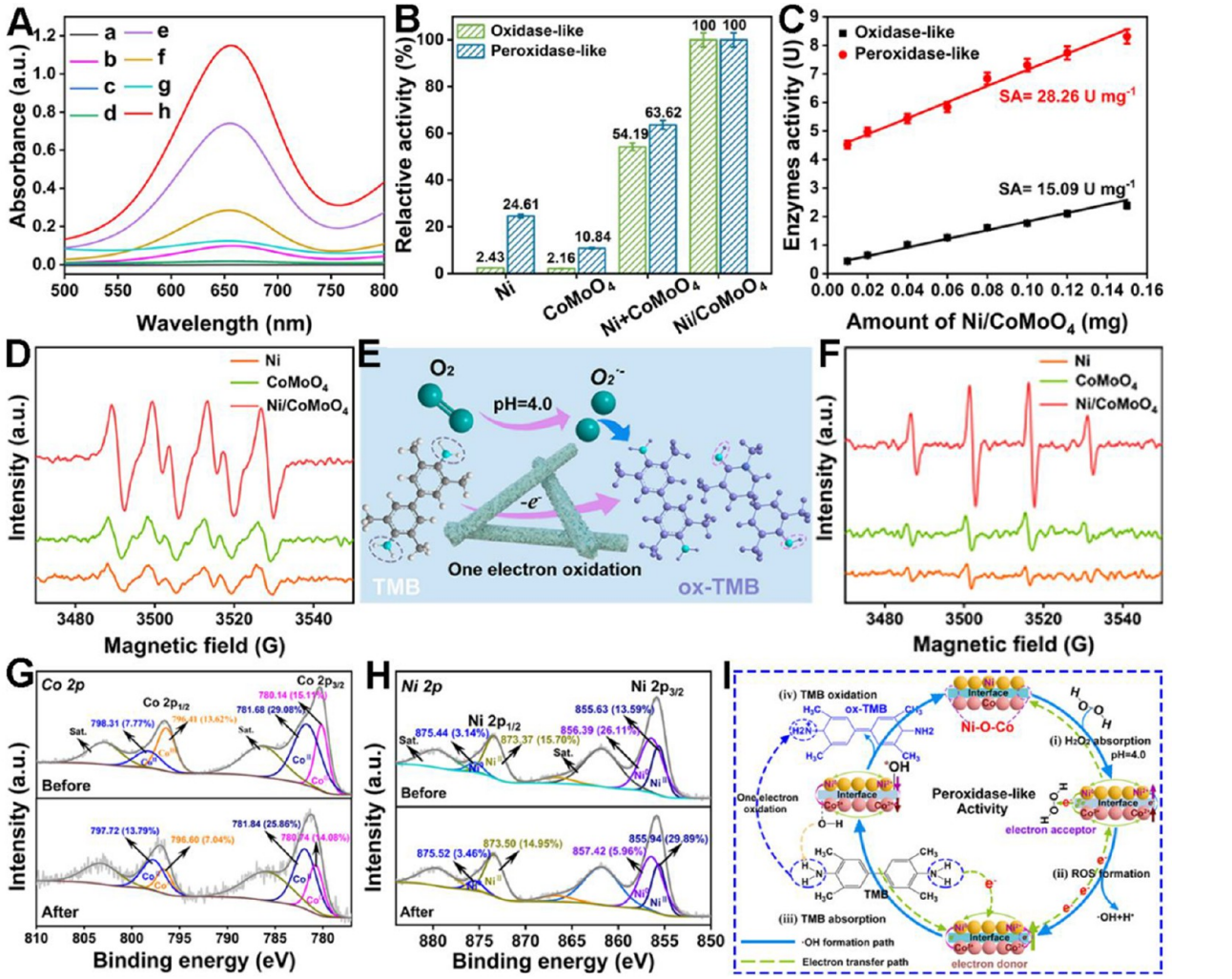

Figure 4. (A) UV−vis absorbance spectra: (a) TMB, (b) H_2O_2/TMB, (c) Ni NPs/TMB, (d) $CoMoO_4$/TMB, (e) Ni/$CoMoO_4$/TMB, (f) Ni NPs/H_2O_2/TMB, (g) $CoMoO_4$/H_2O_2/TMB, and (h) Ni/$CoMoO_4$/H_2O_2/TMB. (B) Relative activity of Ni NPs, $CoMoO_4$, Ni NPs + $CoMoO_4$, and Ni/$CoMoO_4$ for TMB catalysis oxidation in the presence or absence of H_2O_2. (C) Specific activities (SAs) of Ni/$CoMoO_4$ with oxidase-like and peroxidase-like activities. ESR spectra of (D) $O_2^{\bullet-}$ and (F) $^{\bullet}OH$. (E) Possible mechanism for the oxidase-like activity of Ni/$CoMoO_4$. XPS spectra of (G) Ni 2p and (H) Co 2p in Ni/$CoMoO_4$ before and during the reaction. (I) Possible mechanism for the peroxidase-like activity of Ni/$CoMoO_4$.

reasonable that the selected $CoMoO_4$ and Ni possess the essential terms to form the heterostructure model.[57] The addition of Ni was the key driving factor of the interfacial charge redistribution and chemical bond coupling, which could transfer electrons from the Ni to $CoMoO_4$ species through Ni−O−Co bonds (Figure 2G).

Additionally, density functional theory (DFT) was implemented to comprehensively study the electronic structure and interface interaction of Ni−O−Co bonds. All models had no band gap, indicating that their metal properties were conducive to rapid electron transfer in catalysis[25] (Figure 2H). The density of states (DOS) of Ni/$CoMoO_4$ was greater than that of $CoMoO_4$, revealing Ni/$CoMoO_4$ facilitated electron transfer by the heterostructure interface. The Ni/$CoMoO_4$ heterostructure was further clarified by calculating the difference in the electron density (Figure 2I). The yellow and blue regions were the electron accumulation and electron depletion areas, respectively. Significantly, electron redistribution existed in the Ni−O−Co bonds, which was conducive to enhanced electron transfer and modified the reaction kinetics. The electrons shifting from Ni to $CoMoO_4$ led to electron aggregation on $CoMoO_4$ and hole aggregation on Ni, which were consistent with the results of XPS.

The chemical bonding coordination environment and exact electronic structure of Ni/$CoMoO_4$ were thoroughly investigated through X-ray absorption near-edge structure (XANES) spectroscopy. The Co K-edge XANES spectra are displayed in Figure 3A. It is observed that energy of Ni/$CoMoO_4$ is slightly lower than that of $CoMoO_4$. The results imply that the Co species in Ni/$CoMoO_4$ is more declined than that in $CoMoO_4$, demonstrating the electron transfer between Ni and $CoMoO_4$ at the interface. Meanwhile, the near edge absorption of Ni/$CoMoO_4$ indicates that the Co species of $CoMoO_4$ and Ni/$CoMoO_4$ exist as the oxidation state due to the similar signal strength with Co_3O_4 and CoO. As for the Ni K-edge XANES spectra (Figure 3C), the increasing sequence of strength was Ni foil < Ni < Ni/$CoMoO_4$ < NiO, revealing that the valence state of the Ni species in Ni/$CoMoO_4$ was between 0 and +2.

https://doi.org/10.1021/acsnano.1c11012
ACS Nano 2022, 16, 4536−4550

Furthermore, the X-ray absorption fine structure (EXAFS) spectrum and the corresponding fitted results are shown in Figure 3 and Figure S4. There are three obvious peaks corresponding to the Co−O, Co−O−Co, and Co−O−Mo bonds in the Co K-edge EXAFS spectrum of $CoMoO_4$ (Figure 3B). Ni/$CoMoO_4$ has a similar structure to $CoMoO_4$, but an additional peak appeared between Co−O−Co and Co−O−Mo and the amplitude was much stronger than $CoMoO_4$. This indicated that the Co species in Ni/$CoMoO_4$ had higher coordination number than $CoMoO_4$.[58] The fitting results (Table S2) show that the emerged peaks could be attributed to Co−O−Ni bonds, the bond length was 3.09 Å, and the coordination number was 9.0. Meanwhile, the coordination number of Co in the Co−O−Co bonds increased from 4.4 to 9.0 (Co−O−Ni (Co)) due to Ni replacing some Co atoms. Thus, Co−O−Ni bonds might lie in the interface rather than inside the $CoMoO_4$ matrix. It could be deduced that in the synthesis process, a considerable number of OVs were first generated on the surface of $CoMoO_4$ and then the interaction between Ni and $CoMoO_4$ led to the formation of Co−O−Ni bonds.[26]

The Ni species with an oxidation state were found in Ni/$CoMoO_4$ (Figure 3C). Figure 3D displays the Ni K-edge EXAFS spectra of Ni, NiO, and Ni/$CoMoO_4$. Compared with Ni, the two main peaks of Ni/$CoMoO_4$ are significantly enhanced, indicating that it became easier to form Ni−O−Co bonds in Ni after hybridization. Meanwhile, the formation of Ni−O−Co bonds with bond length of 3.05 Å in the heterostructure interface led to an increase in the coordination number of the Ni−O bonds (Table S3). Interestingly, the addition of Ni caused the surface reconstruction of Ni/$CoMoO_4$, and a well-structured electric field was formed at the interface of Ni/$CoMoO_4$, which was conducive to electron transfer through Ni−O−Co bonds. Therefore, the Ni−O−Co bonds played an extremely important role in Ni/$CoMoO_4$ heterostructure catalysis. The wavelet transform (WT) for the k^3-weighted EXAFS signals of the Co K-edge and the Ni K-edge spectra (Figures 3E−H, S5, and S6) also clearly revealed the formation of Co−O−Ni bonds in Ni/$CoMoO_4$. The XANES and EXAFS results as well as the XPS spectra evidenced that there were strong electronic interactions due to the Ni−O−Co bonds between Ni and $CoMoO_4$. This interfacial effect laid a foundation for optimizing the catalytic activity of nanozymes.

Study on Catalytic Propertyies and Steady-State Dynamics. When 3,3',5,5'-tetramethylbenzidine (TMB) changed to the oxidation state TMB (ox-TMB), there was a clear signal peak at 652 nm, accompanied by a color change (colorless to blue). Thus, TMB could be used as a chromogenic substrate for the analysis of enzyme-like activity.[59] Based on the color changes, as shown in Figure 4A, TMB itself was colorless and had no signal peak, and the absorbance values of Ni NPs/TMB and $CoMoO_4$/TMB were also ultralow. However, it should be noted that Ni/$CoMoO_4$ and TMB coexist and there was an obvious UV−visible absorption peak, indicating that Ni/$CoMoO_4$ could directly oxidize TMB to form ox-TMB owing to high oxidase-like activity. Similarly, under the optimal conditions, there was no peak in the H_2O_2/TMB system. Both Ni NPs/H_2O_2/TMB and $CoMoO_4$/H_2O_2/TMB only presented the weak peak at 652 nm due to the extremely low peroxidase-like activity, while Ni/$CoMoO_4$/H_2O_2/TMB with a high-absorption peak showed an excellent catalytic performance. For comparison, the UV−vis absorbance intensity at 652 nm in the Ni/$CoMoO_4$/TMB and Ni/$CoMoO_4$/TMB/H_2O_2 systems was set as a reference (100%), respectively (Figure 4B). The ones in the Ni NPs system were calculated as 2.43%, 24.61% and 2.16%, 10.84% in the $CoMoO_4$ systems, under the systems of oxidase- and peroxidase-like activities, respectively. Obviously, compared with single Ni NPs and $CoMoO_4$, the catalytic activity of Ni/$CoMoO_4$ was improved by 46.2-times and 9.2-times for oxidase-like and peroxidase-like activities. The reason was that the new active sites of Ni−O−Co bonds were formed on the interface of Ni and $CoMoO_4$, which was proved by EXAFS and Raman spectroscopies. They made the contact closer and reduced the interface contacting resistance, and Ni regulated the electron transfer between Co(II) and Co(III), which could improve the peroxidase-like activity. Meanwhile, ESR analysis also showed that the OV content on the surface of Ni/$CoMoO_4$ increased significantly after the addition of Ni (Figure 2C), which was helpful to enhance the oxidase-like activity through OVs. Furthermore, the UV−vis characteristic peak intensity was Ni/$CoMoO_4$/TMB/H_2O_2 > Ni/$CoMoO_4$/TMB. Due to the presence of H_2O_2, the absorption intensity of Ni/$CoMoO_4$/TMB/H_2O_2 at 652 nm was 1.5-times the absorption peak intensity of Ni/$CoMoO_4$/TMB from the oxidase-like activity. Thus, it was proved that Ni/$CoMoO_4$ as the oxidase and peroxidase simulated enzyme activities with specific activities (SAs) of 15.09 and 28.26 U mg^{-1}, respectively (Figure 4C). In order to further evaluate the interaction between Ni NPs and $CoMoO_4$, as shown in Figure 4B, the enzyme-like catalytic properties of mono-Ni NPs and $CoMoO_4$ were determined. In comparison with the mono-Ni NPs or $CoMoO_4$, higher enzyme-like catalytic activities were observed in the corresponding Ni/$CoMoO_4$ nanozymes. Moreover, the enzyme-like catalytic performance of the mixture of mono-Ni NPs + $CoMoO_4$ was significantly weaker than that of the Ni/$CoMoO_4$. These results fully indicated that the close interface between Ni and $CoMoO_4$ promoted the interaction between them, and Ni−O−Co bonds as active site played an important role in the enzymatic reaction. Moreover, to further prove the double enzyme-like activities of Ni/$CoMoO_4$, different oxidation substrates 2, 2'-azino-bis(3-ethylbenzothiazoline-6-sulfonic acid) (ABTS), 1,2-diaminobenzene (OPD) , and p-phenylenediamine (PPD) were explored systemically with or without H_2O_2 (Figure S7). A higher absorption peak of the Ni/$CoMoO_4$/substrate/H_2O_2 system was obtained than that without H_2O_2, proving that Ni/$CoMoO_4$ owned two simulated enzyme activities again. Meanwhile, the pH and Ni/$CoMoO_4$ and TMB concentrations were optimized in Figure S8. It shows that the optimum pH and concentrations of Ni/$CoMoO_4$ and TMB were set as 4.0, 0.05 mg/mL, and 0.17 mM for oxidase-like activity and 4.0, 0.06 mg/mL, and 0.33 mM for peroxidase-like activity, respectively.

The steady-state kinetics of the double enzyme-like activity were determined based on the Michaelis−Menten equation. For the oxidase-like activity, the Lineweaver−Burk double reciprocal curve is shown in Figure S9A, and the Michaelis−Menten constant (k_m) with 0.09 mM was calculated by the Michaelis−Menten equation. As shown in Table S4, in contrast to horseradish peroxidase (HRP) and other nanozymes, the k_m value of Ni/$CoMoO_4$ was the lowest, indicating that it had the highest affinity with the substrate (TMB). Similarly, the steady-state kinetics of the peroxidase-like activity was evaluated using different substrates (TMB and

https://doi.org/10.1021/acsnano.1c11012
ACS Nano 2022, 16, 4536−4550

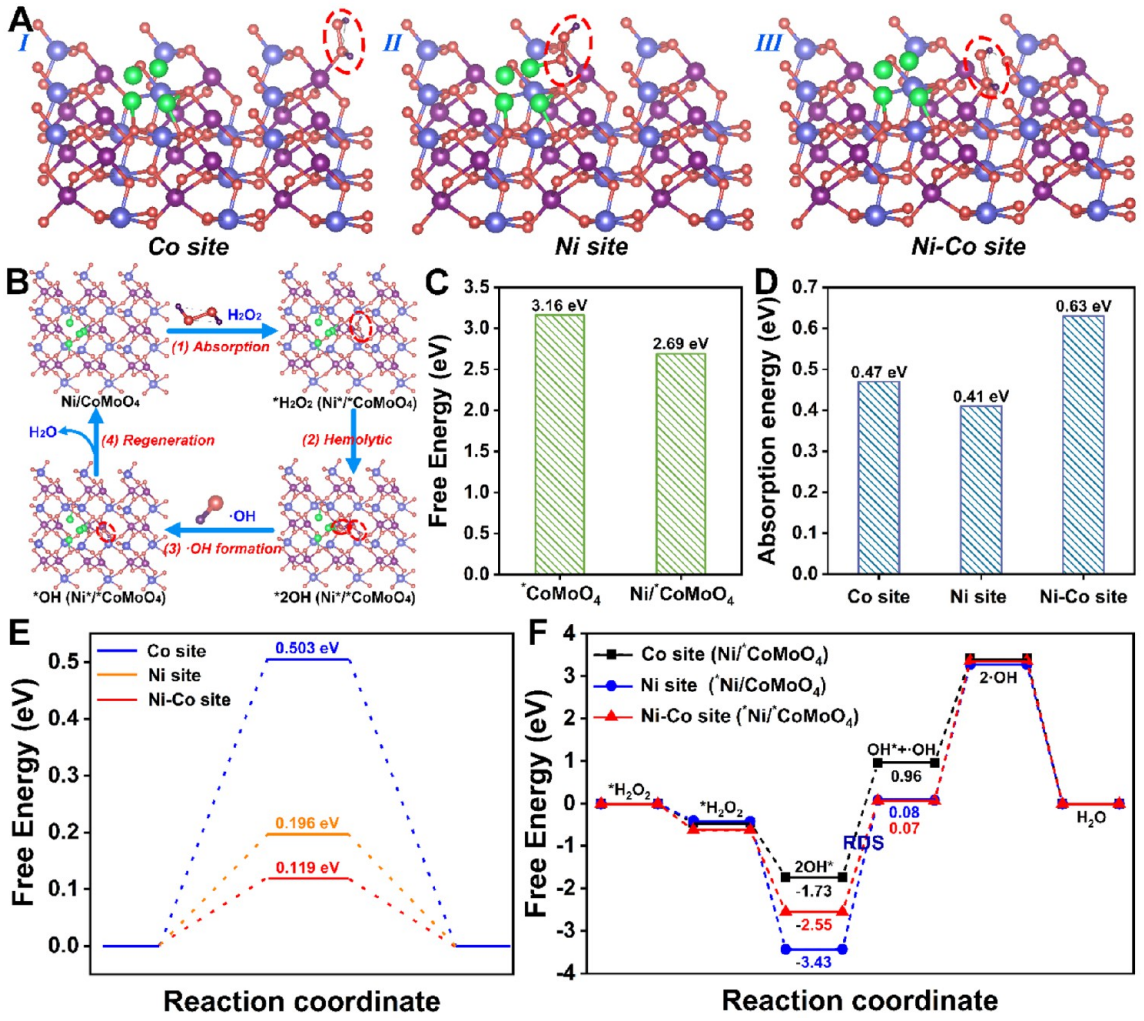

Figure 5. (A) Different adsorption sites of H_2O_2. (B) Proposed reaction process on Ni/$CoMoO_4$. (C) Energy barriers of $CoMoO_4$ and Ni/$CoMoO_4$ in the RDS. (D) Adsorption energy and (E) reaction energy barrier of H_2O_2 dissociation at different sites. (F) Free energy diagram of the reaction process of Ni/$CoMoO_4$ with different adsorption sites.

H_2O_2). Figure S9B shows the reaction rates of different TMB concentrations with fixed H_2O_2 concentration and vice versa (Figure S9C). The steady-state kinetic constant k_m values of TMB and H_2O_2 as substrate were 0.076 and 0.008 mM, respectively, compared with the k_m values of other nanozymes (Table S5), which were lower than most nanozymes. It could be seen that Ni/$CoMoO_4$ had a strong affinity for TMB and H_2O_2.

Study on the Catalytic Mechanism. According to reports, dissolved oxygen was related to the catalytic performance of the oxidase-like activity.[60] To study the influence of O_2 on the oxidase-like activity, the TMB oxidation experiments were implemented under different atmospheric conditions (O_2, air, and N_2), and the absorbance intensity was A_{652nm} (O_2) > A_{652nm} (air) > A_{652nm} (N_2) (Figure S10A). The results proved that O_2 was involved in the oxidation of TMB. Then, diverse concentrations of scavengers including NaN_3, iso-propyl alcohol (IPA), p-benzoquinone (PBQ), and ethylene diamine tetra-acetic acid (EDTA) were used to evaluate the reactive oxygen species (ROS) formation in the process of TMB oxidation. As could be seen from Figure S10B, there was almost no decrease of the oxidase-like activity of Ni/$CoMoO_4$ after the addition of NaN_3 and IPA, showing that no $^1O_2$ and $^{\bullet}OH$ were produced in the oxidation process. On the contrary, the oxidase-like activities were significantly inhibited in the presence of PBQ or EDTA, indicating $O_2^{\bullet-}$ and OVs played an important role in the catalytic process. Besides, the ultralow ESR signals of Ni NPs/5,5-dimethyl-1-pyrroline *N*-oxide (DMPO) and the $CoMoO_4$/DMPO system are presented in Figure 4D. The results show that Ni/$CoMoO_4$/DMPO systems present the obvious signal ratio of 1:1:1:1 due to the formation of $O_2^{\bullet-}$, which was much higher than that of the control group Ni and $CoMoO_4$. Above all, the oxidase-like activity of Ni/$CoMoO_4$ could promote the formation of $O_2^{\bullet-}$ and OVs, which could further oxidize TMB (Figure 4E).

Furthermore, the possible mechanism of Ni/$CoMoO_4$ with peroxidase-like activity in the presence of H_2O_2 was further explored. Due to the strong affinity of H_2O_2 (k_m = 0.08), when H_2O_2 was added into the Ni/$CoMoO_4$/TMB system, H_2O_2 was adsorbed on the surface of Ni/$CoMoO_4$ at first. Then, the O−O bond in H_2O_2 could be decomposed into two $^{\bullet}OH$.[61] A series of control experiments were implemented to verify the $^{\bullet}OH$ formation in the catalytic process. First, different scavengers were used to capture the corresponding ROS, including $O_2^{\bullet-}$, $^1O_2$, and $^{\bullet}OH$. It could be seen from Figure S11, after adding a certain concentration of thiourea (TH) to

https://doi.org/10.1021/acsnano.1c11012
ACS Nano 2022, 16, 4536−4550

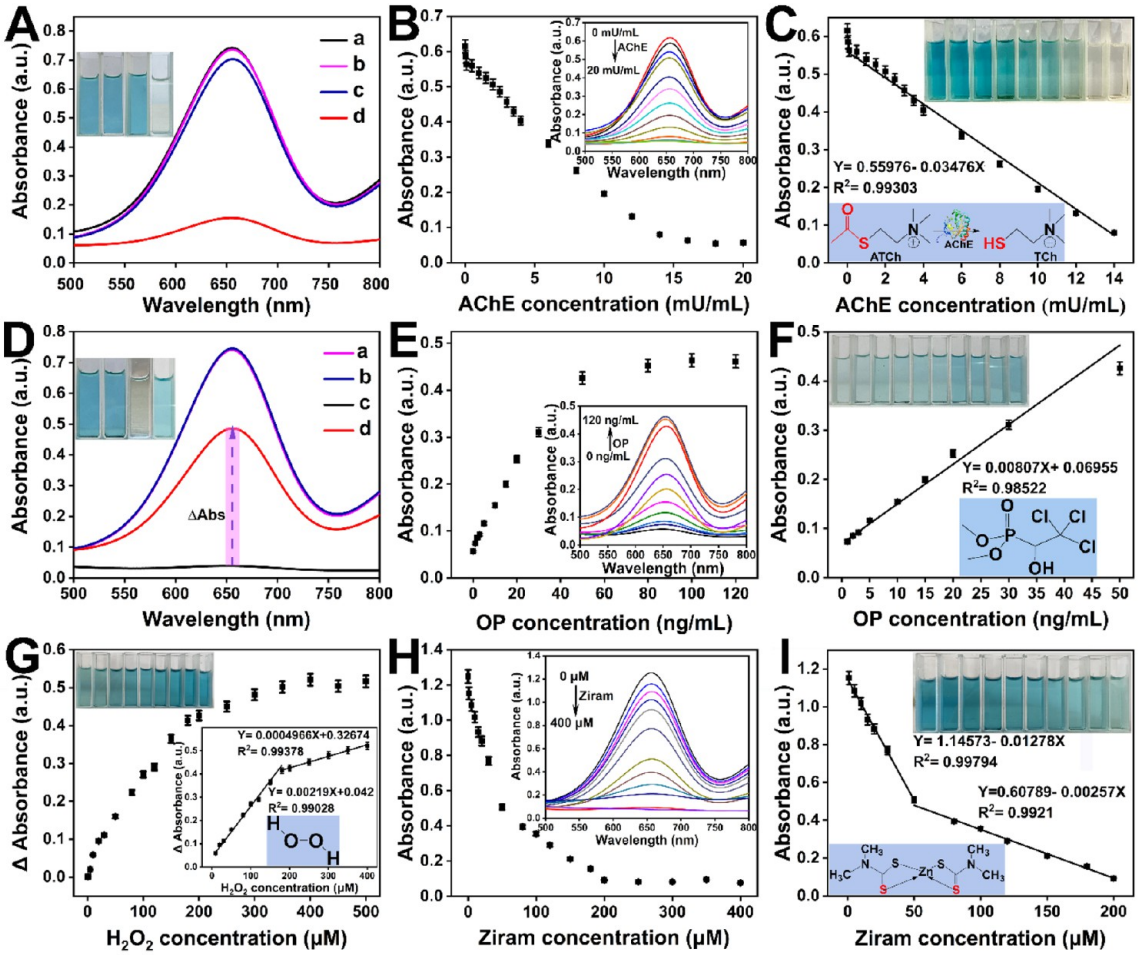

Figure 6. (A) UV−vis absorption spectrum of (a) the Ni/$CoMoO_4$/TMB system with (b) ATCh, (c) AChE, and (d) ATCh + AChE. (B) Relationship between absorbance and AChE concentration. (C) Linear calibration plot of AChE in the range 0.01−14 mU mL^{-1}. (D) UV−vis absorption spectrum of (a) the Ni/$CoMoO_4$/TMB system with (b) OP, (c) ATCh + AChE, and (d) ATCh + AChE + OP. (E) Relationship between absorbance and OP concentration. (F) Linear calibration plot of trichlorfon in the range 1−50 ng mL^{-1}. (G) Relationship between absorbance change (ΔA652) and H_2O_2 concentration. (H) Relationship between absorbance and ziram concentration. (I) Linear calibration plot of ziram in the range 1−200 μM (Inset: corresponding photographs of reaction solution).

the reaction system, the its relative catalytic activity decreased significantly due to the scavenging effect of TH on $^{\bullet}OH$. This proved that Ni/$CoMoO_4$ could catalyze H_2O_2 to produce $^{\bullet}OH$. Similarly, ESR spectroscopy also had been used to directly detect the formation of $^{\bullet}OH$ during the peroxidase-like catalysis. It exhibited that the intensity of a visible ESR signal with a 1:2:2:1 quartet was Ni/$CoMoO_4$ > Ni NPs > $CoMoO_4$ (Figure 4F). There was no doubt that Ni/$CoMoO_4$ could catalyze the reaction of H_2O_2 to more $^{\bullet}OH$. The above results further testify that Ni/$CoMoO_4$ could effectively enhance the production of ROS, contributing to the higher catalytic activity.

To further understand the electron transfer mechanism, the XPS results of Ni and Co in Ni/$CoMoO_4$ before and during the reaction in the Ni/$CoMoO_4$/H_2O_2/TMB system were analyzed (Figure 4G and H). The peak position of Co 2p did not change obviously during the reaction, but the surface ratio of Co^{2+}/Co^{3+} increased significantly. Meanwhile, the ratio of Ni^0/Ni^{2+} on the surface decreased obviously, which indicated Ni^0 could transfer electrons to Co^{3+} and convert itself to Ni^{2+}, making Co^{3+} change to Co^{2+}. Besides, the tight interface formed by the Ni/$CoMoO_4$ heterostructure could enhance the electron transfer between Ni and Co, resulting in rapid reaction kinetics, which significantly improved its enzyme-like activity (A_{652nm} = 0.74 without H_2O_2, A_{652nm} = 1.15 with H_2O_2). In addition, Cytochrome C (Cyt C), as an electron transporter, was used to verify the electron accepting ability of Ni/$CoMoO_4$. When Cyt C existed alone, two obvious characteristic peaks at 520 and 550 nm were assigned to the reduced state of Cyt C. However, the two original characteristic peaks disappeared when Cyt C and Ni/$CoMoO_4$ coexisted. And the special signal of the oxidized Cyt C was found at 530 nm. These results proved that Ni/$CoMoO_4$ could obtain electrons from Cyt C (Figure S12A). Moreover, the fact that electron transfer could enhance the peroxidase-like activity of Ni/$CoMoO_4$ was further confirmed by the electrochemical response (Figure S12B). Before measurement, Ni/$CoMoO_4$ was fixed onto the surface of a glassy carbon electrode, and no obvious current response was observed. Significantly, there was an apparent current response of about 140 μA in the presence of H_2O_2. This phenomenon clearly illustrated that Ni/$CoMoO_4$ had the ability of electron transfer between Ni/$CoMoO_4$ (electron donor) and H_2O_2 substrate (electron acceptor).[62] These results further confirm that Ni/$CoMoO_4$ could promote the reaction between H_2O_2 and TMB. Combined with the XPS results, the relationship between

https://doi.org/10.1021/acsnano.1c11012
ACS Nano 2022, 16, 4536−4550

electron transfer and peroxidase-like activity could be explained as follows. In the process of peroxidase-like catalysis, H_2O_2 was adsorbed on the surface of Ni/$CoMoO_4$ first, and then the electrons of Ni^0-O-Co^{3+} over Ni/$CoMoO_4$ would be transferred to H_2O_2, which could accelerate the key step of the reaction ($^1/_2H_2O_2 \rightarrow {}^{\bullet}OH$). As for the active sites of Ni/$CoMoO_4$, the Ni^0-O-Co^{3+} bond would change to $Ni^{2+}-O-Co^{2+}$ due to losing an electron to H_2O_2 and the other electron transfer from Ni^0 to Co^{3+}. This is the reason why the content of Ni^{2+} and Co^{2+} increased during the peroxidase-like reaction. Then TMB was adsorbed on the surface of Ni/$CoMoO_4$, and the lone pair electrons on the amino group were donated to $Ni^{2+}-O-Co^{2+}$, which made $Ni^{2+}-O-Co^{2+}$ recover to the Ni^0-O-Co^{3+} state before reaction.[63,64] It would accelerate the transfer of electrons from Ni^0-O-Co^{3+} to H_2O_2 (Figure 4I). Thus, the ability of electron transfer from Ni/$CoMoO_4$ to H_2O_2 would enhance the peroxidase-like activity.

The density functional theory (DFT) calculations were carried out for an in-depth explanation of the active sites of H_2O_2 reduction by Ni/$CoMoO_4$. The adsorbed model of H_2O_2 on different active sites (Co sites, Ni sites, and Ni−Co sites) is revealed in Figure 5A. The reaction process of catalyzing H_2O_2 is displayed in Figures S13A and 5B. The H_2O_2 was first adsorbed on the active site, and then the activated H_2O_2 was dissociated homogeneously to two −OH*, one of which desorbed from the adsorbed site to form the ${}^{\bullet}OH$, which was used as the rate-determining step (RDS). The other adsorbed hydroxyl would react with protonated hydrogen atoms to form H_2O molecules. After that, the catalyst recovered to its initial state after H_2O desorption. The reaction process energy diagrams of $CoMoO_4$ and Ni/$CoMoO_4$ are shown in Figure S13B, and the Gibbs free energy (ΔG) of Ni/$CoMoO_4$ in the RDS was notably lower than that of $CoMoO_4$ (Figure 5C). This was because the Ni−O−Co bond formation of Ni/$CoMoO_4$ accelerated the kinetics of the nanozyme catalyzed reaction. Furthermore, the energy absorbed by different active sites is shown in Figure 5D; the adsorption energies of H_2O_2 on Co sites, Ni sites, and Ni−Co sites were −0.47, −0.41, and −0.63 eV, respectively. This indicated that the Ni−Co site had the highest adsorption capacity for H_2O_2, which was advantageous to improve the catalytic activity. And the Ni−Co sites had a lower energy barrier when they catalyzed the decomposition of H_2O_2 to 2OH* (Figure 5E), indicating that Ni−Co sites had a stronger ability to decompose H_2O_2 than Ni sites and Co sites. This showed that there was an effective electron transfer at the heterojunction interface due to the covalent interaction among Co, Ni, and O (Co−O−Ni). Besides, it is worth noting that the energy change of the RDS is Ni−Co sites (2.62 eV) < Co sites (2.69 eV) < Ni sites (3.51 eV) (Figures 5F and S14). Thus, this implies that the O atom in the Ni−O−Co bonds might easily obtain electrons from Ni to modify the electronic structure of $CoMoO_4$, resulting in enhance peroxidase-like activity. Hence, the higher catalytic capacity of Ni/$CoMoO_4$ was compactly relevant with its higher capacity of adsorbing H_2O_2 (higher adsorption energy) and generation of ${}^{\bullet}OH$ (lower energy barrier). Meanwhile, the excellent enzyme-like properties of Ni/$CoMoO_4$ mainly came from the formation of Ni and $CoMoO_4$ heterointerfaces.

Colorimetric Biosensor Analysis of Acetylcholinesterase (AChE) and Trichlorfon Based on Oxidase-like Activity. As Lewis base, thiol molecules were easily coordinated with metal atoms, which could block the catalytic active sites and inhibit the TMB oxidation over Ni/$CoMoO_4$.[65] Based on the above, mercapto molecules, such as glutathione (GSH) and L-cysteine (Cys), were used to investigate their effects on the oxidase-like activities of Ni/$CoMoO_4$ (Supporting Information). To further broaden the analytical performance of Ni/$CoMoO_4$ nanozymes, a colorimetric biological platform for visual detection of acetylcholinesterase (AChE) was constructed. Under optimal conditions (Figure S17), the control experiment shown in Figure 6A, the addition of AChE alone or ATCh had little effect on the activity of Ni/$CoMoO_4$ nanozymes. However, it is worth noting that the A_{652nm} decreases significantly by about 80% when both AChE and ATCh coexist in system. It is because AChE could quickly hydrolyze ATCh to TCh, and the product TCh with a similar thiol structure of Cys and GSH (Figure S18) could block the active sites of Ni/$CoMoO_4$. In addition, with the addition of AChE, the absorbance value (A_{652nm}) decreased gradually (Figure 6B). There is a fine linear relationship between A_{652nm} and the AChE concentration in the range 0.01−14 mU mL^{-1} (Y = 0.55976−0.03476X, R^2 = 0.99303) (Figure 6C). And the limit of detection (LOD) was calculated to be 0.006 mU mL^{-1} through $3\sigma/b$ (S/N = 3), where σ and b were the standard deviation of the blank control and the slope of the corresponding calibration curve, respectively. Compared with the reported methods (Table S6), the AChE sensor constructed by this method was comparable and even better than other methods, indicating this sensor had good sensitivity.

Organophosphorus (OP) is used as a pesticide all over the world, which irreversibly inhibits the activity of AChE and, thus, causes loss of the ability to decompose ATCh. Considering the effect of the inhibition of OP, an on−off−on biosensor based on Ni/$CoMoO_4$ was constructed further for the detection of trichlorfon (a typical OP). The absorbance peak remained unchanged after adding OP in the Ni/$CoMoO_4$/TMB system, which indicated that the effect of OP on the Ni/$CoMoO_4$ + TMB reaction system could be ignored (Figure 6D). But the peak obviously increased after adding OP into the Ni/$CoMoO_4$/TMB/AChE/ATCh system. This was because the addition of different concentrations of OP would gradually inactivate AChE, which weakened the inhibition and provided a stronger absorption signal for the biosensor (Figure 6E). Compared with the reported methods (Table S7), this biosensor exhibited a good linear relationship between A_{652nm} and the trichlorfon concentration from 1 to 50 ng mL^{-1} with an extremely low LOD of 0.35 ng mL^{-1} (Figure 6F). In addition, the selectivity of the colorimetric sensing system was further evaluated in the detection of complex samples (Supporting Information).

Colorimetric Biosensor Analysis of H_2O_2 and Ziram Based on Peroxidase-like Activity. A convenient and rapid H_2O_2 colorimetric analysis platform was devised in Figure 6G. The absorbance value of ox-TMB (652 nm) was proportional to the H_2O_2 concentration from 10 to 400 μM. The linear relations were obtained to be Y = 0.00219X + 0.042 and Y = 0.0004966X + 0.32674, and the LOD was 5.22 μM. Compared to the previously reported methods in Table S8, the Ni/$CoMoO_4$ with the excellent peroxidase-like activity presented high sensitivity, which would provide a great potential for quantitative analysis of H_2O_2. Besides, to further broaden the analytical property of Ni/$CoMoO_4$, the inhibition ability for ziram was investigated. And the colorimetric detection of ziram was rarely reported. The UV−vis results of Ni/$CoMoO_4$/

https://doi.org/10.1021/acsnano.1c11012
ACS Nano 2022, 16, 4536−4550

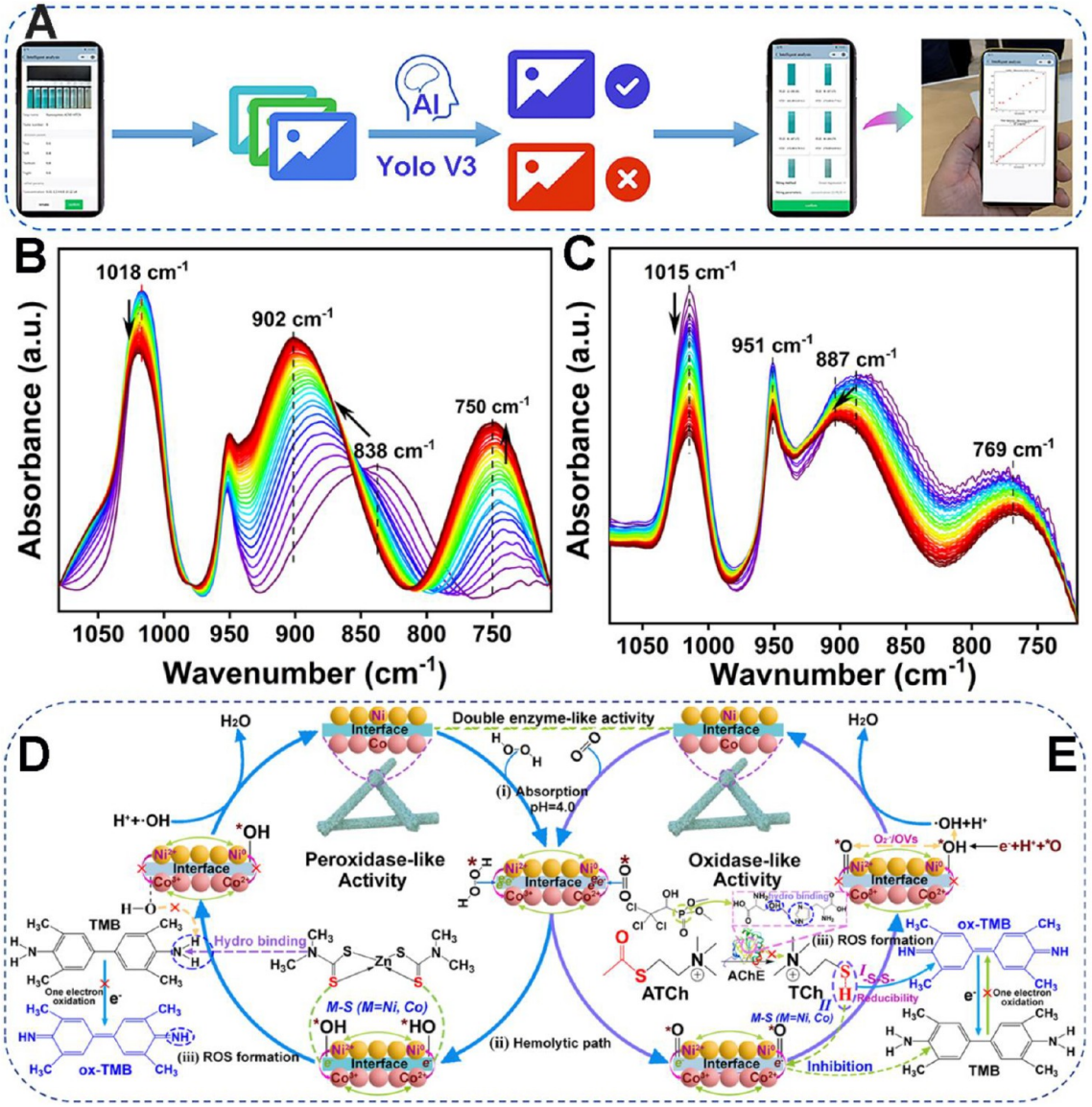

Figure 7. (A) Prediction stage of the deep learning model. (B and C) Time-dependent *in situ* FTIR spectra of detection of target molecules. Detection mechanism of target molecules based on the peroxidase-like (D) and oxidase-like (E) activities.

TMB/H_2O_2 before and after adding ziram are displayed in Figure 6H. It showed that the absorbance was obviously decreased after adding ziram. Moreover, the absorbance intensity was directly proportional to the ziram concentration (1−200 μM) and the LOD was 0.33 μM (Figure 6I). Compared with other colorimetric methods reported (Table S9), the sensor showed better sensitivity and satisfactory specificity. Additionally, the constructed colorimetric platform had good practicability and feasibility for the detection of AChE and pesticide residue. It was of great significance to detect actual samples in food and the environmental field (Supporting Information). Besides, in order to further confirm the stability of the sensing system, the repeatability and stability of nanozymes were further evaluated (Supporting Information).

Smartphone Biosensor Analysis of Target Molecules Based on Deep Learning. Furthermore, a portable smartphone platform combining an intelligent analysis App based on deep learning and a colorimetric signal was structured for convenient and visual detection of target molecules. The App adopted the Yolo V3 target detection algorithm (Figure S19). Through in-depth learning, the input image was automatically recognized, and the self-designed color pattern analysis App was used to analyze the color of the output "useful" photos to create a statistical model (Figure 7A). Then the Yolo V3 algorithm of the self-developed App was used to segment the image and extract the average value of RGB or HSV. Subsequently, the relationship between the average value of red, green and blue (RGB) or hue, saturation and value (HSV) and the target molecule concentration was fitted by a linear support vector machine (SVM). Finally, a (G+R)/B model was chosen owing to its fine linear relationship, and the fitting equation $Y = 0.074X + 1.0673$ ($R^2 = 0.9897$) was automatically presented on the smartphone screen (Figure S20A). Similarly, as shown in Figure S20B, a portable smartphone analysis biosensor for the detection of OP had also been structured. Based on the calculated the R, G, B and H, S, V values, the different modes were obtained intelligently.

https://doi.org/10.1021/acsnano.1c11012
ACS Nano 2022, 16, 4536−4550

Compared with other models, the G model had a good linear relationship with the OP concentration, and the fitting equation was Y = 107.4978 − 0.7275X with R^2 = 0.9897. As shown in Figure S20C, the G/B model was chosen for detecting ziram because of its good linear fitting equation Y = 0.0013X + 0.8273 (R^2 = 0.9906). Therefore, a visual and convenient intelligent biosensor based on deep learning for the on-site detection of target molecules without complex instruments was structured.

Detection Mechanism of Target Molecules. The S 2p XPS spectrum after reaction with ziram presented two peaks at 162.01 and 163.21.0 eV, which were assigned to S $2p_{3/2}$ and S $2p_{1/2}$, respectively (Figure S21). This was indicated as metal sulfide (M−S, M = Ni, Co) formation,[66] and the Co−S bonds were observed at 164.12 eV,[67] which further proved that ziram blocked the Ni−O−Co bonds and reduced the catalytic reaction kinetics. Furthermore, the detection mechanism was further studied by *in situ* FTIR. It was could see from Figure 7B that the band at 1018 cm^{-1} was related to the C═S(−S) stretching vibrations. The band intensity decreased monotonically and the wavenumber moved slightly with the detection time. This may be due to the interaction between ziram and Ni/$CoMoO_4$. Moreover, it could be clearly observed that the band at 838 cm^{-1} (Ni−O−Co) moved significantly to 902 cm^{-1}, which further confirmed the strong interaction between ziram and Ni/$CoMoO_4$. This not only greatly shortened the distance of the M−S bonds but also covered some active sites on the catalyst surface. However, the peak at 750 cm^{-1} was attributed to the vibrational peak of the MoO_4 tetrahedral units.[68] It could be observed that with the increase of detection time, the absorption peak intensity increased significantly and the wavenumber also shifted slightly. The above results further proved that the interaction between ziram and Ni/$CoMoO_4$ occurred in the Ni−O−Co bonds at the interface rather than $CoMoO_4$.[69] Thus, the disappearance of Ni−O−Co bonds further blocked the electron transfer at the heterostructure interface and decreased the kinetics of the catalytic reaction. Besides, XPS analysis also showed that Ni^0 accounted for 14.63% and the Co^{2+}/Co^{3+} ratio was 1.03 in the Ni/$CoMoO_4$/H_2O_2/TMB system (Figure S22A and B*I*). However, after adding ziram into the above system, the Ni^0 content on the surface of Ni/$CoMoO_4$ increased significantly, and the Co^{2+}/Co^{3+} ratio was calculated to be 0.63 (Figure S22A and B*II*). This was because the formation of the M−S bonds decreased the catalytic capacity of the Ni−O−Co active sites due to the complexation of ziram with Co formation.

Similarly, the mechanism of TCh detection was thoroughly studied by *in situ* FTIR. The peak at 887 cm^{-1} obviously moved to 903 cm^{-1}, which indicated that the Ni−O−Co bonds had a strong interaction with the TCh. This would block the active site of Ni−O−Co. The vibration bands at 951 and 769 cm^{-1} belonged to the Mo−O−Mo bond and the distorted MoO_4 tetrahedron, respectively.[68] The C−S stretching vibrations at 1015 cm^{-1} decreased significantly, while the peak at 769 cm^{-1} increased, which may be due to the formation of the M−S bond at the heterojunction interface. Moreover, after adding OP to the Ni/$CoMoO_4$/AChE/ATCh/TMB system, the UV−vis spectral intensity increased significantly at 652 nm (Figure 6D), which was due to the fact that the OPs could poison AChE and inhibit the formation of TCh. In addition, in the Ni/$CoMoO_4$/AChE/ATCh/TMB system, the content of Ni^{2+} and the ratio of Co^{2+}/Co^{3+} (0.54) decreased significantly (Figure S22A and B*III*), compared to the Ni/$CoMoO_4$/TMB system. This was the reason that the interaction between the sulfhydryl group and Ni−O−Co reduced the electron transfer between Ni and Co. Oppositely, after the addition of OP, the content of Ni^0 increased and the Co^{2+}/Co^{3+} ratio increased to 1.39 due to the inhibition of AChE (Figure S22A and B*IV*), which restored the Ni−O−Co interaction and ensured sufficient active sites.

The possible catalytic mechanism was displayed based on the above analysis and discussion (Figure 7). The peroxidase-like activity of Ni/$CoMoO_4$ was attributed to electron transfer of Ni−O−Co bonds at the interface promoting $^{\bullet}OH$ production, while the oxidase-like activity was because of rich OVs on the surface of Ni/$CoMoO_4$ and $O_2^{\bullet-}$ production. Therefore, the "on−off−on" reaction systems were successfully constructed due to the different enzyme-like activities. Figure 7D displays the catalytic mechanism for the detection of ziram. Due to its symmetrical structure and active sulfur atom, ziram was easy to coordinate with metal elements to form an M−S (M = Ni, Co) bond. Meanwhile, the two methyl groups were bound to the nitrogen atom, which had a strong electron donating property. Besides, the electronegative atom of ziram would form a hydrogen bond with the amino group of TMB, which blocked the oxidation of TMB by $^{\bullet}OH$. Thus, compared with the Ni/$CoMoO_4$/H_2O_2/TMB system (A_{652nm} = 1.25), the absorbance intensity of the Ni/$CoMoO_4$/H_2O_2/TMB/ziram system decreased significantly (A_{652nm} = 0.07), which was affirmed by UV−vis spectroscopy (inset of Figure 6H).

For the application of oxidase-like detection, an "on−off−on" colorimetric biosensor was constructed. As shown in Figure 7E, AChE could rapidly hydrolyze ATCh to form TCh, which contains mercaptan molecules. On the one hand, the -SH groups dehydrogenated to form a disulfide bond, which was reductive and reduced ox-TMB (Figure 7E(*I*)). On the other hand, -SH groups coordinate with metal atoms to form M-S bonds, which blocked the electrons transfer at the heterojunction interface and reduced the catalytic oxidation of TMB (Figure 7Eii).

CONCLUSION

In conclusion, with the help of a large number of Ni−O−Co bonds, the Ni/$CoMoO_4$ heterostructure displayed outstanding double enzyme-like activity properties. Compared with the single Ni NPs and $CoMoO_4$, the catalytic activities of the oxidase-like and peroxidase-like enzymes of Ni/$CoMoO_4$ were increased by 46.2-fold and 9.2-fold, with SAs of 15.09 and 28.26 U mg^{-1} respectively. Additionally, both experiments and DFT calculations supplied a better comprehension of the catalytic mechanism and revealed the important role of interface engineering in enhancing the activity. Subsequently, colorimetric and intelligent detection systems based on deep learning were constructed. For oxidase activity, AChE and OP pesticides could be simultaneously detected based on signal "on−off−on" changes. The detection mechanism revealed that the produced TCh containing -SH could inhibit bimetallic catalytic active sites (Ni−O−Co), while the addition of OP could damage the active sites of AChE, thus blocking the production of TCh. Similarly, based on peroxidase-like enzymes, the linear range of ziram was 1−200 μM. And *in situ* FTIR spectroscopy systematically revealed that ziram interacted strongly with Ni−O−Co bonds to form M−S (M = Ni, Co) bonds; thus, it would block the active site. This work not only determined the structure−activity relationship of nanozymes but also thoroughly studied the detection

https://doi.org/10.1021/acsnano.1c11012
ACS Nano 2022, 16, 4536−4550

mechanism for ziram and AChE. The advantages of the synergistic effect of reasonable design defects and the interface electronic structure were revealed and provided a fairly good design principle for the development of advanced nanozyme catalysts.

METHODS

Synthesis of Ni/$CoMoO_4$. In the previous work, $CoMoO_4$ was successfully synthesized by the hydrothermal method.[9] Subsequently Ni/$CoMoO_4$ was synthesized by *in situ* chemical reduction. Briefly, 0.0387 g of $NiCl_2{\cdot}6H_2O$ and prepared $CoMoO_4$ (0.04 g) were dissolved in deionized water (20 mL), and the resulting solution was stirred for 3 h. Then $NaHB_4$ (10 mL, 10 mg·mL^{-1}) was added slowly, and stirring was continued for 5 h. Finally, Ni/$CoMoO_4$ was gained through centrifugation and washing with ultrapure water and ethanol for three times and then drying at 80 °C.

Oxidase-like Activity Assay. The uniformly dispersed aqueous solution of Ni/$CoMoO_4$ or $CoMoO_4$ (2 mg mL^{-1}, 80 μL) was added to the acetate buffer solution (ABS, pH= 4.0, 3 mL total volume) with 5 mM TMB. Finally, the mixture was incubated at 37 °C for 25 min. Then the absorbance intensity was measured with a UV visible spectrophotometer. In order to obtain optimal conditions, the influence of pH and TMB and material concentrations on the oxidase-like activity was studied.

Peroxidase-like Activity Assay. In order to detect Ni/$CoMoO_4$, $CoMoO_4$, and Ni with peroxidase-like activity, the absorbance was recorded in ABS containing the material (90 μL, 2 mg mL^{-1}) and 5 mM TMB along with 10 mM H_2O_2. The next assay was similar to oxidase-like activity assay.

ASSOCIATED CONTENT

Supporting Information

The Supporting Information is available free of charge at https://pubs.acs.org/doi/10.1021/acsnano.1c11012.

All characterization analyses (XRD, XPS, SEM, TEM, FTIR, Raman, XANES, ICP-MS, ESR, etc.), measurements of enzyme-like activity and specific activity (SA), calculation of corresponding parameters, DFT calculation details, multifunctional application, smartphone biosensor analysis, and some discussion details (Figures S1−S28 and Tables S1−S12) (PDF)

AUTHOR INFORMATION

Corresponding Authors

Qingbiao Zhao − *Key Laboratory of Polar Materials and Devices, Ministry of Education, Department of Electronic Science, East China Normal University, Shanghai 200241, China*; Email: qbzhao@ee.ecnu.edu.cn

Hanbing Rao − *College of Science, Sichuan Agricultural University, Ya'an 625014, China*; orcid.org/0000-0003-2453-2426; Email: rhb@sicau.edu.cn

Mengmeng Sun − *College of Science, Sichuan Agricultural University, Ya'an 625014, China*; orcid.org/0000-0003-0177-1723; Email: sunmeng14391@163.com

Authors

Yang Dang − *College of Science, Sichuan Agricultural University, Ya'an 625014, China*

Guangtu Wang − *College of Science, Sichuan Agricultural University, Ya'an 625014, China*

Gehong Su − *College of Science, Sichuan Agricultural University, Ya'an 625014, China*; orcid.org/0000-0002-9849-5632

Zhiwei Lu − *College of Science, Sichuan Agricultural University, Ya'an 625014, China*

Yanying Wang − *College of Science, Sichuan Agricultural University, Ya'an 625014, China*

Tao Liu − *College of Information Engineering, Sichuan Agricultural University, Ya'an 625014, China*

Xiang Pu − *College of Science, Sichuan Agricultural University, Ya'an 625014, China*; orcid.org/0000-0003-1439-8657

Xianxiang Wang − *College of Science, Sichuan Agricultural University, Ya'an 625014, China*; orcid.org/0000-0001-6234-2231

Chun Wu − *College of Science, Sichuan Agricultural University, Ya'an 625014, China*

Chang Song − *School of Arts and Media, Sichuan Agricultural University, Ya'an 625014, China*

Complete contact information is available at: https://pubs.acs.org/10.1021/acsnano.1c11012

Notes

The authors declare no competing financial interest.

ACKNOWLEDGMENTS

The authors acknowledge the financial support of this work by the Science and Technology Program of Sichuan Province (Grant Nos. 2021YJ0316, 2021YFG0250, and 2021YJ0343), the National Natural Science Foundation of China (Grant No. 22104102, 21905186), and Two-Way Support Team Programs of Sichuan Agricultural University (Project No. 2021993036).

REFERENCES

(1) Wei, H.; Wang, E. Nanomaterials with Enzyme-Like Characteristics (Nanozymes): Next-Generation Artificial Enzymes. *Chem. Soc. Rev.* **2013**, *42*, 6060−6093.

(2) Wei, H.; Gao, L.; Fan, K.; Liu, J.; He, J.; Qu, X.; Dong, S.; Wang, E.; Yan, X. Nanozymes: A Clear Definition with Fuzzy Edges. *Nano Today* **2021**, *40*, 101269.

(3) Huang, Y.; Ren, J.; Qu, X. Nanozymes: Classification, Catalytic Mechanisms, Activity Regulation, and Applications. *Chem. Rev.* **2019**, *119*, 4357−4412.

(4) Chong, Y.; Liu, Q.; Ge, C. Advances in Oxidase-Mimicking Nanozymes: Classification, Activity Regulation and Biomedical Applications. *Nano Today* **2021**, *37*, 101076.

(5) Jiang, D.; Ni, D.; Rosenkrans, Z. T.; Huang, P.; Yan, X.; Cai, W. Nanozyme: New Horizons for Responsive Biomedical Applications. *Chem. Soc. Rev.* **2019**, *48*, 3683−3704.

(6) Tang, G.; He, J.; Liu, J.; Yan, X.; Fan, K. Nanozyme for Tumor Therapy: Surface Modification Matters. *Exploration* **2021**, *1*, 75−89.

(7) Liang, X.; Han, L. White Peroxidase-Mimicking Nanozymes: Colorimetric Pesticide Assay without Interferences of O_2 and Color. *Adv. Funct. Mater.* **2020**, *30*, 2001933.

(8) Wang, J.; Huang, R.; Qi, W.; Su, R.; Binks, B. P.; He, Z. Construction of a Bioinspired Laccase-Mimicking Nanozyme for the Degradation and Detection of Phenolic Pollutants. *Appl. Catal. B Environ.* **2019**, *254*, 452−462.

(9) Sun, M.; Dang, Y.; Du, R.; Lu, Z.; Wang, Y.; Wang, X.; Song, C.; Liu, T.; Wang, G.; Ye, J.; et al. Experiment and Theoretical Insights into CuNi/$CoMoO_4$ Multi-Functional Catalyst with Laccase-Like: Catalysis Mechanism, Smartphone Biosensing and Organic Pollutant Efficient Degradation. *Chem. Eng. J.* **2021**, *425*, 130586.

(10) Gao, M.; Wang, Z.; Zheng, H.; Wang, L.; Xu, S.; Liu, X.; Li, W.; Pan, Y.; Wang, W.; Cai, X.; et al. Two-Dimensional Tin Selenide (SnSe) Nanosheets Capable of Mimicking Key Dehydrogenases in Cellular Metabolism. *Angew. Chem., Int. Ed.* **2020**, *59*, 3618−3623.

(11) Lu, Z.; Dang, Y.; Dai, C.; Zhang, Y.; Zou, P.; Du, H.; Zhang, Y.; Sun, M.; Rao, H.; Wang, Y. Hollow MnFeO Oxide Derived From MOF@MOF with Multiple Enzyme-Like Activities for Multifunction Colorimetric Assay of Biomolecules and Hg^{2+}. *J. Hazard. Mater.* **2021**, *403*, 123979.

(12) Liu, Q.; Zhang, A.; Wang, R.; Zhang, Q.; Cui, D. A Review on Metal- and Metal Oxide-Based Nanozymes: Properties, Mechanisms, and Applications. *Nano-Micro Lett.* **2021**, *13*, 154.
(13) Luo, L.; Su, Z.; Zhuo, J.; Huang, L.; Nian, Y.; Su, L.; Zhang, W.; Wang, J. Copper-Sensitized "Turn On" Peroxidase-Like Activity of $MMoO_4$ (M = Co, Ni) Flowers for Selective Detection of Aquatic Copper Ions. *ACS Sustainable Chem. Eng.* **2020**, *8*, 12568−12576.
(14) Wang, X.; Gao, X. J.; Qin, L.; Wang, C.; Song, L.; Zhou, Y. N.; Zhu, G.; Cao, W.; Lin, S.; Zhou, L.; et al. e_g Occupancy As an Effective Descriptor for the Catalytic Activity of Perovskite Oxide-Based Peroxidase Mimics. *Nat. Commun.* **2019**, *10*, 704.
(15) Zhou, Y.; Wei, Y.; Ren, J.; Qu, X. A Chiral Covalent Organic Framework (COF) Nanozyme with Ultrahigh Enzymatic Activity. *Mater. Horiz.* **2020**, *7*, 3291−3297.
(16) Xi, J.; Zhang, R.; Wang, L.; Xu, W.; Liang, Q.; Li, J.; Jiang, J.; Yang, Y.; Yan, X.; Fan, K.; et al. A Nanozyme-Based Artificial Peroxisome Ameliorates Hyperuricemia and Ischemic Stroke. *Adv. Funct. Mater.* **2021**, *31*, 2007130.
(17) Cao, F.; Zhang, L.; Wang, H.; You, Y.; Wang, Y.; Gao, N.; Ren, J.; Qu, X. Defect-Rich Adhesive Nanozymes As Efficient Antibiotics for Enhanced Bacterial Inhibition. *Angew. Chem., Int. Ed.* **2019**, *58*, 16236−16242.
(18) Xu, C.; Qu, X. Cerium Oxide Nanoparticle: a Remarkably Versatile Rare Earth Nanomaterial for Biological Applications. *NPG Asia Materials* **2014**, *6*, e90−e90.
(19) Wang, Z.; Zhang, R.; Yan, X.; Fan, K. Structure and Activity of Nanozymes: Inspirations for *de novo* Design of Nanozymes. *Mater. Today* **2020**, *41*, 81−119.
(20) Shen, L.; Che, Q.; Li, H.; Zhang, X. Mesoporous $NiCo_2O_4$ Nanowire Arrays Grown on Carbon Textiles as Binder-Free Flexible Electrodes for Energy Storage. *Adv. Funct. Mater.* **2014**, *24*, 2630−2637.
(21) Li, M.; Xu, S.; Cherry, C.; Zhu, Y.; Wu, D.; Zhang, C.; Zhang, X.; Huang, R.; Qi, R.; Wang, L.; et al. Hierarchical 3-Dimensional $CoMoO_4$ Nanoflakes on a Macroporous Electrically Conductive Network with Superior Electrochemical Performance. *J. Mater. Chem. A* **2015**, *3*, 13776−13785.
(22) Chen, P.; Tong, Y.; Wu, C.; Xie, Y. Surface/Interfacial Engineering of Inorganic Low-Dimensional Electrode Materials for Electrocatalysis. *Acc. Chem. Res.* **2018**, *51*, 2857−2866.
(23) Zhang, Y.; Lin, Y.; Duan, T.; Song, L. Interfacial Engineering of Heterogeneous Catalysts for Electrocatalysis. *Mater. Today* **2021**, *48*, 115−134.
(24) Wu, Y.; Xu, W.; Jiao, L.; Tang, Y.; Chen, Y.; Gu, W.; Zhu, C. Defect Engineering in Nanozymes. *Mater. Today* **2021**. DOI: 10.1016/j.mattod.2021.10.032.
(25) Wang, T.; Wang, P.; Zang, W.; Li, X.; Chen, D.; Kou, Z.; Mu, S.; Wang, J. Nanoframes of Co_3O_4-Mo_2N Heterointerfaces Enable High-Performance Bifunctionality toward Both Electrocatalytic HER and OER. *Adv. Funct. Mater.* **2022**, *32*, 2107382.
(26) Zhao, G.; Li, P.; Cheng, N.; Dou, S. X.; Sun, W. An Ir/$Ni(OH)_2$ Heterostructured Electrocatalyst for the Oxygen Evolution Reaction: Breaking the Scaling Relation, Stabilizing Iridium(V), and Beyond. *Adv. Mater.* **2020**, *32*, 2000872.
(27) Hou, Y.; Lohe, M. R.; Zhang, J.; Liu, S.; Zhuang, X.; Feng, X. Vertically Oriented Cobalt Selenide/NiFe Layered-Double-Hydroxide Nanosheets Supported on Exfoliated Graphene Foil: an Efficient 3D Electrode for Overall Water Splitting. *Energy Environ. Sci.* **2016**, *9*, 478−483.
(28) Sun, H.; Li, J.; Lv, L.; Li, Z.; Ao, X.; Xu, C.; Xue, X.; Hong, G.; Wang, C. Engineering Hierarchical CoSe/NiFe Layered-Double-Hydroxide Nanoarrays As High Efficient Bifunctional Electrocatalyst for Overall Water Splitting. *J. Power Sources* **2019**, *425*, 138−146.
(29) Luo, W.; Jiang, C.; Li, Y.; Shevlin, S. A.; Han, X.; Qiu, K.; Cheng, Y.; Guo, Z.; Huang, W.; Tang, J. Highly Crystallized α-FeOOH for a Stable and Efficient Oxygen Evolution Reaction. *J. Mater. Chem. A* **2017**, *5*, 2021−2028.
(30) Li, J.; Gu, Y.; Sun, H.; Lv, L.; Li, Z.; Ao, X.; Xue, X.; Hong, G.; Wang, C. Engineering the Coupling Interface of Rhombic Dodecahedral NiCoP/C@FeOOH Nanocages toward Enhanced Water Oxidation. *Nanoscale* **2019**, *11*, 19959−19968.
(31) Gao, M.-R.; Liang, J.-X.; Zheng, Y.-R.; Xu, Y.-F.; Jiang, J.; Gao, Q.; Li, J.; Yu, S.-H. An Efficient Molybdenum Disulfide/Cobalt Diselenide Hybrid Catalyst for Electrochemical Hydrogen Generation. *Nat. Commun.* **2015**, *6*, 5982.
(32) Gong, K.; Du, F.; Xia, Z.; Durstock, M.; Dai, L. Nitrogen-Doped Carbon Nanotube Arrays with High Electrocatalytic Activity for Oxygen Reduction. *Science* **2009**, *323*, 760−764.
(33) Liu, G.; Robertson, A. W.; Li, M. M. J.; Kuo, W. C. H.; Darby, M. T.; Muhieddine, M. H.; Lin, Y. C.; Suenaga, K.; Stamatakis, M.; Warner, J. H.; et al. MoS_2 Monolayer Catalyst Doped with Isolated Co Atoms for the Hydrodeoxygenation Reaction. *Nat. Chem.* **2017**, *9*, 810−816.
(34) Li, Y. J.; Cui, L.; Da, P. F.; Qiu, K. W.; Qin, W. J.; Hu, W. B.; Du, X. W.; Davey, K.; Ling, T.; Qiao, S. Z. Multiscale Structural Engineering of Ni-Doped CoO Nanosheets for Zinc-Air Batteries with High Power Density. *Adv. Mater.* **2018**, *30*, 1804653.
(35) Zhao, S.; Wang, Y.; Dong, J.; He, C.-T.; Yin, H.; An, P.; Zhao, K.; Zhang, X.; Gao, C.; Zhang, L.; et al. Ultrathin Metal-Organic Framework Nanosheets for Electrocatalytic Oxygen Evolution. *Nat. Energy* **2016**, *1*, 16184.
(36) Jiang, J.; Sun, F.; Zhou, S.; Hu, W.; Zhang, H.; Dong, J.; Jiang, Z.; Zhao, J.; Li, J.; Yan, W.; et al. Atomic-Level Insight into Super-Efficient Electrocatalytic Oxygen Evolution on Iron and Vanadium Co-doped Nickel (oxy)hydroxide. *Nat. Commun.* **2018**, *9*, 2885.
(37) Liu, Y.; Hua, X.; Xiao, C.; Zhou, T.; Huang, P.; Guo, Z.; Pan, B.; Xie, Y. Heterogeneous Spin States in Ultrathin Nanosheets Induce Subtle Lattice Distortion to Trigger Efficient Hydrogen Evolution. *J. Am. Chem. Soc.* **2016**, *138*, 5087−5092.
(38) Zhou, M.; Lu, F.; Shen, X.; Xia, W.; He, H.; Zeng, X. One-Pot Construction of Three Dimensional $CoMoO_4/Co_3O_4$ Hybrid Nanostructures and Their Application in Supercapacitors. *J. Mater. Chem. A* **2015**, *3*, 21201−21210.
(39) Shi, J.; Li, X.; He, G.; Zhang, L.; Li, M. Electrodeposition of High-Capacitance 3D CoS/Graphene Nanosheets on Nickel Foam for High-Performance Aqueous Asymmetric Supercapacitors. *J. Mater. Chem. A* **2015**, *3*, 20619−20626.
(40) Xia, X.; Lei, W.; Hao, Q.; Wang, W.; Wang, X. One-Step Synthesis of $CoMoO_4$/Graphene Composites with Enhanced Electrochemical Properties for Supercapacitors. *Electrochim. Acta* **2013**, *99*, 253−261.
(41) Wang, B.; Cao, Y.; Chen, Y.; Wang, R.; Wang, X.; Lai, X.; Xiao, C.; Tu, J.; Ding, S. Microwave-Assisted Fast Synthesis of Hierarchical $NiCo_2O_4$ Nanoflower-Like Supported $Ni(OH)_2$ Nanoparticles with an Enhanced Electrocatalytic Activity Towards Methanol Oxidation. *Inorg. Chem. Front.* **2018**, *5*, 172−182.
(42) Rodriguez, M.; Stolzemburg, M. C. P.; Bruziquesi, C. G. O.; Silva, A. C.; Abreu, C. G.; Siqueira, K. P. F.; Oliveira, L. C. A. S.; Pires, M. S.; Lacerda, L. C. T.; Ramalho, T. C.; et al. Electrocatalytic Performance of Different Cobalt Molybdate Structures for Water Oxidation in Alkaline Media. *CrystEngComm* **2018**, *20*, 5592−5601.
(43) Ji, D.; Fan, L.; Tao, L.; Sun, Y.; Li, M.; Yang, G.; Tran, T. Q.; Ramakrishna, S.; Guo, S. The Kirkendall Effect for Engineering Oxygen Vacancy of Hollow Co_3O_4 Nanoparticles toward High-Performance Portable Zinc-Air Batteries. *Angew. Chem., Int. Ed.* **2019**, *58*, 13840−13844.
(44) Li, Q.; Zhao, Y.; Liu, H.; Xu, P.; Yang, L.; Pei, K.; Zeng, Q.; Feng, Y.; Wang, P.; Che, R. Dandelion-Like Mn/Ni Co-doped CoO/C Hollow Microspheres with Oxygen Vacancies for Advanced Lithium Storage. *ACS Nano* **2019**, *13*, 11921−11934.
(45) Wang, M.; Cui, Y.; Cao, H.; Wei, P.; Chen, C.; Li, X.; Xu, J.; Sheng, G. Activating Peroxydisulfate with $Co_3O_4/NiCo_2O_4$ Double-shelled Nanocages to Selectively Degrade Bisphenol A-A Nonradical Oxidation Process. *Appl. Catal. B Environ.* **2021**, *282*, 119585.
(46) Lu, Z.; Zhang, Y.; Sun, M.; Zou, P.; Wang, X.; Wang, Y.; Huang, Q.; Chen, H.; Ye, J.; Rao, H. N-doped Carbon Dots Regulate Porous Hollow Nickel-Cobalt Sulfide: High-Performance Electrode

Materials in Supercapacitor and Enzymeless Glucose Sensor. *J. Power Sources* **2021**, *516*, 230685.
(47) Sun, M.; Huang, S.; Su, G.; Wang, X.; Lu, Z.; Wang, Y.; Liu, T.; Jiang, Y.; Song, C.; Rao, H. Synthesis of pH-Switchable Pt/Co_3O_4 Nanoflowers: Catalytic Mechanism, Four-enzyme Activity and Smartphone Biosensing Applications. *Chem. Eng. J.* **2022**, *437*, 134414.
(48) Zhang, B.; Wang, L.; Zhang, Y.; Ding, Y.; Bi, Y. Ultrathin FeOOH Nanolayers with Abundant Oxygen Vacancies on $BiVO_4$ Photoanodes for Efficient Water Oxidation. *Angew. Chem., Int. Ed.* **2018**, *57*, 2248−2252.
(49) Du, Y.; Xue, J.; Sun, X.; Wu, D.; Liu, X.; Ju, H.; Yang, L.; Wei, Q. Oxygen Vacancy-Enhanced Electrochemiluminescence Sensing Strategy Using Luminol Thermally Encapsulated in Apoferritin As a Transducer for Biomarker Immunoassay. *Anal. Chem.* **2020**, *92*, 8472−8479.
(50) Hu, T.; Wang, Y.; Zhang, L.; Tang, T.; Xiao, H.; Chen, W.; Zhao, M.; Jia, J.; Zhu, H. Facile Synthesis of PdO-doped Co_3O_4 Nanoparticles As an Efficient Bifunctional Oxygen Electrocatalyst. *Appl. Catal. B Environ.* **2019**, *243*, 175−182.
(51) Xu, L.; Jiang, Q.; Xiao, Z.; Li, X.; Huo, J.; Wang, S.; Dai, L. Plasma-Engraved Co_3O_4 Nanosheets with Oxygen Vacancies and High Surface Area for the Oxygen Evolution Reaction. *Angew. Chem., Int. Ed.* **2016**, *55*, 5277−5281.
(52) Soundharrajan, V.; Sambandam, B.; Song, J.; Kim, S.; Jo, J.; Kim, S.; Lee, S.; Mathew, V.; Kim, J. $Co_3V_2O_8$ Sponge Network Morphology Derived from Metal-Organic Framework As an Excellent Lithium Storage Anode Material. *ACS Appl. Mater. Interfaces* **2016**, *8*, 8546−8553.
(53) Weng, X.; Guo, M.; Luo, F.; Chen, Z. One-Step Green Synthesis of Bimetallic Fe/Ni Nanoparticles by Eucalyptus Leaf Extract: Biomolecules Identification, Characterization and Catalytic Activity. *Chem. Eng. J.* **2017**, *308*, 904−911.
(54) Yuan, J.; Cheng, X.; Wang, H.; Lei, C.; Pardiwala, S.; Yang, B.; Li, Z.; Zhang, Q.; Lei, L.; Wang, S.; et al. A Superaerophobic Bimetallic Selenides Heterostructure for Efficient Industrial-Level Oxygen Evolution at Ultra-High Current Densities. *Nano-Micro Lett.* **2020**, *12*, 104.
(55) Sun, J.; Xue, H.; Guo, N.; Song, T.; Hao, Y.-r.; Sun, J.; Zhang, J.; Wang, Q. Synergetic Metal Defect and Surface Chemical Reconstruction into $NiCo_2S_4$/ZnS Heterojunction to Achieve Outstanding Oxygen Evolution Performance. *Angew. Chem., Int. Ed.* **2021**, *60*, 19435−19441.
(56) Xu, H.; Zhang, Z.; Liu, J.; Do-Thanh, C.-L.; Chen, H.; Xu, S.; Lin, Q.; Jiao, Y.; Wang, J.; Wang, Y.; et al. Entropy-Stabilized Single-Atom Pd Catalysts *via* High-Entropy Fluorite Oxide Supports. *Nat. Commun.* **2020**, *11*, 3908.
(57) Wang, X.; Zhan, G.; Wang, Y.; Zhang, Y.; Zhou, J.; Xu, R.; Gai, H.; Wang, H.; Jiang, H.; Huang, M. Engineering Core-Shell Co_9S_8/Co Nanoparticles on Reduced Graphene Oxide: Efficient Bifunctional Mott-Schottky Electrocatalysts in Neutral Rechargeable Zn-Air Batteries. *Journal of Energy Chemistry* **2022**, *68*, 113.
(58) Sun, J.; Xu, W.; Lv, C.; Zhang, L.; Shakouri, M.; Peng, Y.; Wang, Q.; Yang, X.; Yuan, D.; Huang, M.; et al. Co/MoN Hetero-Interface Nanoflake Array with Enhanced Water Dissociation Capability Achieves the Pt-Like Hydrogen Evolution Catalytic Performance. *Appl. Catal. B Environ.* **2021**, *286*, 119882.
(59) Zhang, X.; Yang, Q.; Lang, Y.; Jiang, X.; Wu, P. Rationale of 3, 3′, 5, 5′-Tetramethylbenzidine As the Chromogenic Substrate in Colorimetric Analysis. *Anal. Chem.* **2020**, *92*, 12400−12406.
(60) Wu, Y.; Jiao, L.; Luo, X.; Xu, W.; Wei, X.; Wang, H.; Yan, H.; Gu, W.; Xu, B. Z.; Du, D.; et al. Oxidase-Like Fe-N-C Single-Atom Nanozymes for the Detection of Acetylcholinesterase Activity. *Small* **2019**, *15*, 1903108.
(61) Jiao, L.; Wu, J.; Zhong, H.; Zhang, Y.; Xu, W.; Wu, Y.; Chen, Y.; Yan, H.; Zhang, Q.; Gu, W.; et al. Densely Isolated FeN_4 Sites for Peroxidase Mimicking. *ACS Catal.* **2020**, *10*, 6422−6429.
(62) Mu, J.; Wang, Y.; Zhao, M.; Zhang, L. Intrinsic Peroxidase-Like Activity and Catalase-Like Activity of Co_3O_4 Nanoparticles. *Chem. Commun.* **2012**, *48*, 2540−2542.
(63) Song, Y.; Qu, K.; Zhao, C.; Ren, J.; Qu, X. Graphene Oxide: Intrinsic Peroxidase Catalytic Activity and Its Application to Glucose Detection. *Adv. Mater.* **2010**, *22*, 2206−2210.
(64) Shi, W.; Wang, Q.; Long, Y.; Cheng, Z.; Chen, S.; Zheng, H.; Huang, Y. Carbon Nanodots As Peroxidase Mimetics and Their Applications to Glucose Detection. *Chem. Commun.* **2011**, *47*, 6695−6697.
(65) Ni, P.; Sun, Y.; Dai, H.; Lu, W.; Jiang, S.; Wang, Y.; Li, Z.; Li, Z. Prussian Blue Nanocubes Peroxidase Mimetic-based Colorimetric Assay for Screening Acetylcholinesterase Activity and Its Inhibitor. *Sens Actuators B Chem.* **2017**, *240*, 1314−1320.
(66) Kumari, S.; Chowdhury, A.; Khan, A. A.; Hussain, S. Controlled Surface Functionalization of Ni-S Nanostructures for pH-Responsive Selective and Superior Pollutants Adsorption. *J. Hazard. Mater.* **2021**, *415*, 125750.
(67) He, S.; Du, H.; Wang, K.; Liu, Q.; Sun, J.; Liu, Y.; Du, Z.; Xie, L.; Ai, W.; Huang, W. Low-Temperature Molten Salt Synthesis of MoS_2@CoS_2 Heterostructures for Efficient Hydrogen Evolution Reaction. *Chem. Commun.* **2020**, *56*, 5548−5551.
(68) Chen, H.; Hu, H.; Han, F.; Liu, J.; Zhang, Y.; Zheng, Y. $CoMoO_4$/Bamboo Charcoal Hybrid Material for High-Energy-Density and High Cycling Stability Supercapacitors. *Dalton Trans.* **2020**, *49*, 10799−10807.
(69) Wang, X.; Liu, Y.; Zhang, T.; Luo, Y.; Lan, Z.; Zhang, K.; Zuo, J.; Jiang, L.; Wang, R. Geometrical-Site-Dependent Catalytic Activity of Ordered Mesoporous Co-Based Spinel for Benzene Oxidation: *In Situ* DRIFTS Study Coupled with Raman and XAFS Spectroscopy. *ACS Catal.* **2017**, *7*, 1626−1636.

https://doi.org/10.1021/acsnano.1c11012
ACS Nano 2022, 16, 4536−4550